# DESIGN AND DEVELOPMENT OF A MULTI-DEGREE-OF-FREEDOM NANOPOSITIONING SYSTEM FOR SELF-ASSEMBLY-BASED NANOMANUFACTURING OF DNA PATTERNS

By

GREGORY AUGUSTUS MASTROIANNI

A thesis submitted to the

Graduate School-New Brunswick

Rutgers, The State University of New Jersey

in partial fulfillment of the requirements

for the degree of

Master of Science

Graduate Program in Mechanical and Aerospace Engineering

written under the direction of

Qingze Zou, Ph.D.

and approved by

_____

_____

_____

_____

New Brunswick, New Jersey

January, 2014

# ABSTRACT OF THE THESIS

Design and development of a multi-degree-of-freedom nanopositioning system for self-assembly-based nanomanufacturing of DNA patterns

by GREGORY AUGUSTUS MASTRIOANNI

Thesis Director:

Qingze Zou, Ph.D.

This thesis presents the design, development, and control of multi-degree-of-freedom nanopositioning stage for applications in self-assembly-based nanomanufacturing of DNA patterns. High speed nanopositioning is needed in a variety of applications, such as nanomanufacture and construction. Particularly, nanopositioning developed in this work can be utilized to study the effect that inducing nano- to micro- scale oscillations in the DNA pattern self-assembly process has on the fabrication efficiency and quality. A system was designed to provide three degrees of freedom that provides both versatility and positioning precision to the study of the self-assembly process. Actual component manufacture was completed for two dimensional motions, with the third dimension

designed for concept. Piezoelectric bimorph actuators were chosen for their low cost and high precision positioning to provide motion to the system. For the applications of the bimorph actuators in multi-dimensional positioning however, adverse effects, including the vibration dynamics and the nonlinear hysteresis behavior of the actuators, challenge the precision tracking of the desired trajectory. Moreover, incorporating multiple degrees of freedom inherits an undesirable cross-axis dynamics coupling effect between two or more directions of motion. In this project, two recently-developed iterative control techniques, the modeling-free inverse-based iterative control (MIIC) and the high-order difference modeling-free iterative control (HODMIIC) techniques were comparatively studied through experiments to tackle these critical issues. These two techniques were compared through their use in controlling one-dimensional non-coupled motion trajectories of a variety of amplitude and frequency conditions. The superior HODMIIC algorithm is then further proven through successful control of two-dimensional coupled motion trajectories across similar amplitude and frequencies.

## Acknowledgments

First acknowledgment goes to the advisor and Thesis Director, Professor Zou. I do not forget from where came my desire to study control systems and inspiration to continue my university education, all those semesters ago in the course Vibrations & Controls. I do not forget all help and guidance Professor Zou always selflessly gave both inside and outside of the classroom. Professor Zou offered support not only as an academic coach, but in many important ways, a life coach as well. To my advisor I give my sincerest thanks and gratitude.

Secondly, I would like to give my thanks and gratitude to members of my MS Defense Committee, Professors Yi and Mazzeo. For your willingness to help make my MS Degree come to fruition, and your anticipated constructive criticisms following my defense presentation, I thank you very much. Your efforts and advice can only further hone my academic and communication skill, something for which I am very grateful.

Thirdly, to my friends and fellow graduate colleagues, especially Zhihua Wang, Marlon Avellan, Charlie Kawcynski, Hadi Halim, and Dan Manzo. Zhihua provided guidance with persistent patience at the expense of personal time. For this, I will always be grateful. Charlie, Marlon, Hadi, and Dan were always there to help talk over matters, be them related to academics or otherwise. I honor them for being the truest of friends.

## Dedication

To my cousin Josh. I love and cherish you as a brother.

## Table of Contents

ABSTRACT OF THE THESIS ..... ii

Acknowledgments ..... iv

Dedication ..... v

1. Introduction ..... 1

1.1 Goal ..... 1

1.2 Objectives ..... 2

1.3 Motivation & Challenges ..... 2

2. Design & Development of the Mechanical System ..... 4

2.1 Overview ..... 4

2.2 Mechanical Design & Development ..... 7

2.2.1 Developing a General Plant Model ..... 7

***Dynamics Model of the Positioning Stage*** ..... 9

***Dynamics Model of the Positioning Probe*** ..... 14

2.2.2 Optimal Selection of Bimorphs ..... 16

2.2.3 *Stage* Design & Manufacture ..... 20

***Design*** ..... 20

***Manufacture*** ..... 27

2.2.4 Silicon Wafer Manufacture ..... 27

2.2.5 *Probe* Design & Manufacture ..... 28

***Design*** ..... 28

***Manufacture*** ..... 30

2.2.6 *Base* Design & Manufacture ..... 30

***Design*** ..... 30

***Manufacture*** ..... 33

2.2.7 *X Mount* Design & Manufacture ..... 34

***Design*** ..... 34

***Manufacture*** ..... 36

2.2.8 *Z Mount* & *Z Sensor Rail* Design & Manufacture ..... 36

***Design*** ..... 36

***Manufacture*** ..... 39

2.3 Electrical Design & Development ..... 40

2.3.1 Overview of Objectives ..... 40

2.3.2 Sensing System Design ..... 40

2.3.3 Conditioning Circuit Design ..... 43

***Signal Follower Overview*** ..... 46

***Level Shifter Overview*** ..... 47

***Active Filter & Amplifier Overview*** ..... 47

3. Implementation & Evaluation of Advanced Iterative Learning Control Techniques 49

3.1 Overview of Objectives ..... 49

3.2 Control Law Approach ..... 49

3.3 Implementation & Evaluation ..... 54

3.3.1 Control Law Implementation ..... 54

3.3.2 Plant Dynamics ..... 59

3.3.3 Tracking Results & Discussion ..... 64

***Single-Axis Positioning Results*** ..... 64

***Dual-Axis Positioning Results*** ..... 74

4. Conclusion ..... 78

Appendix A. List of System Components ..... 79

Appendix B. Reflective Object Sensor ..... 84

Appendix C. Operational Amplifier ..... 87

Appendix D. Level Shifter Design ..... 88

Appendix E. Active Filter & Amplifier Design ..... 92

Appendix F. Dual-Axis Motion Error Plots ..... 96

References ..... 99

# 1. Introduction

## 1.1 Goal

The goal of this project was to design and develop a multi-degree-of-freedom precision positioning *Stage* for applications such as self-assembly based nanomanufacturing of DNA patterns [1]. With the increasing miniaturization of electronics, nanostructures are projected to become integral in future technology and nanotechnology developments. DNA can, in the right form, be a useful biomaterial in assisting the construction of nanostructures. To be useful, the DNA should be formed into highly ordered strands. A proven technique of producing these strands based in self-assembly involves allowing a drop of solution containing DNA solute to evaporate from a sphere-on-flat geometry. Many works have produced results of highly ordered gradient concentric DNA ring strands [2, 3].

This project offers a novel development to the basic static experimentation design for DNA self-assembly nanomanufacturing. By introducing multi-degree-of-freedom vibration into the evaporation of the DNA-solution droplet, various unique patterns of highly ordered DNA strands may exist. High-speed nanopositioning control can be implemented, as previously shown through use of piezoelectric actuators [4]. By successful control of three-space vibration over a range of different motions, a plethora of unique patters of DNA strands should exist. This increase in ordered DNA pattern diversity means an increase in nanostructure foundations which, in turn, expands the resulting diversity of nanostructures offered in nanomanufacturing.

## 1.2 Objectives

There were multipart objectives focused on to achieve the project goal. The first objective was to design and build a physical system/ hardware which could both provide dynamic motion to an evaporating droplet of DNA in three degrees of freedom, and sense/quantify the motion. This included design and construction of both a mechanical plant and electrical control/signal processing circuit.

The second objective was to implement and evaluate two novel iterative learning control algorithms for precision nanopositioning at both high-speed (up to 25 Hertz) and relatively large displacement range (up to 1 millimeter). The target waveform to control in this project was triangular. Although this system can be applied with sinusoidal waveforms, the quasi-non-differentiable nature of a triangle wave makes it more difficult to control and thus a suitable candidate for testing the limits of the control system.

## 1.3 Motivation & Challenges

The motivation lies in offering a cost-effective mechanical and electrical design which would meet the underlying project goals. However there are numerous challenges regarding the compensation of existing adverse effects.

The nanopositioning feature lies in the concept of piezoelectric actuation. From the standpoint of the piezoelectric actuator, there are many adverse effects which challenge successful implementation and operation. The vibration dynamics of the piezoelectric actuator can be excited for motion of high-speed and with frequencies

which approach the resonant frequency. Piezoelectric actuators are also affected by a nonlinear hysteresis effect prominent when the actuator is displaced near its limits [5, 6]. In the actuators attempt to track a predetermined trajectory, larger tracking errors are induced as trajectory amplitude and frequency are increased. The success of tracking also suffers from uncertainties and variations in the behavior of the piezoelectric actuator. For example, the piezoelectric actuator suffers from the formation of micro cracks and de-polarization over time as well as behavior variations due to environmental conditions such as temperature and humidity. This speaks to the aging of the actuator and the accompanied adverse effects.

In addition to actuator challenges, challenges arise from the aim to offer three degrees of actuation motion. For such multi-axis positioning, there is an inherent cross-axis dynamics-coupling effect which can arise from misalignment of the actuators and/or positioning sensors [5, 6]. Such cross-axis dynamics coupling effects can contribute significant positioning errors in general for piezoelectric-actuator-based positioning systems [7].Compensation for such coupling was a critical challenge to overcome when considering implementation of the iterative learning control algorithms for precision system control.

# 2. Design & Development of the Mechanical System

## 2.1 Overview

The design objectives were as follows. A system was to be developed to provide precision positioning in three axes, either separately or simultaneously, and utilize this *Stage* to provide controlled vibration either horizontally or vertically to the controlled evaporation process of a DNA solution droplet and arrive at patterns of self-assembled DNA strands. The resulting oscillations should range between 0 and 25 Hertz with peak amplitudes up to 1 millimeter and have a nanometer-level resolution. Additionally, the system must be able to operate in normal room conditions and have a shelf life of at least one year. Easily replaceable parts should be used whenever possible in order to prolong shelf life.

A PC-based data acquisition system involving a high-voltage amplifier and analog signal processing and filtering circuitry was used to drive and measure the displacements via infrared sensors. The solidifying aim was to investigate advanced control algorithms alongside the MATLAB programming language and the Simulink software package to analyze and control the system behavior.

The overall integrated system is represented by the diagram of Fig. 1. Fig. 2 shows a SolidWorks 2012 rendering of the final physical plant.

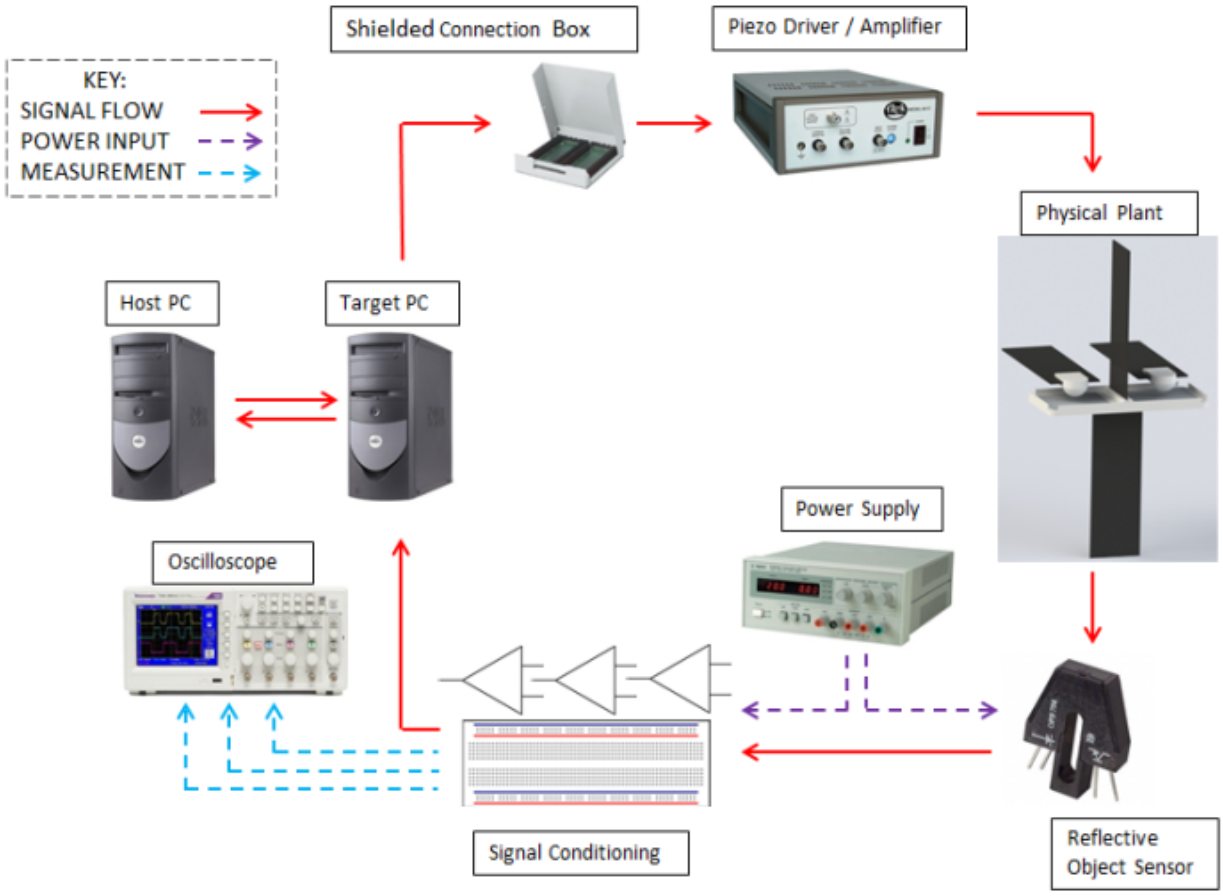


Fig. 1. Mechanical and electrical system signal flow overview.

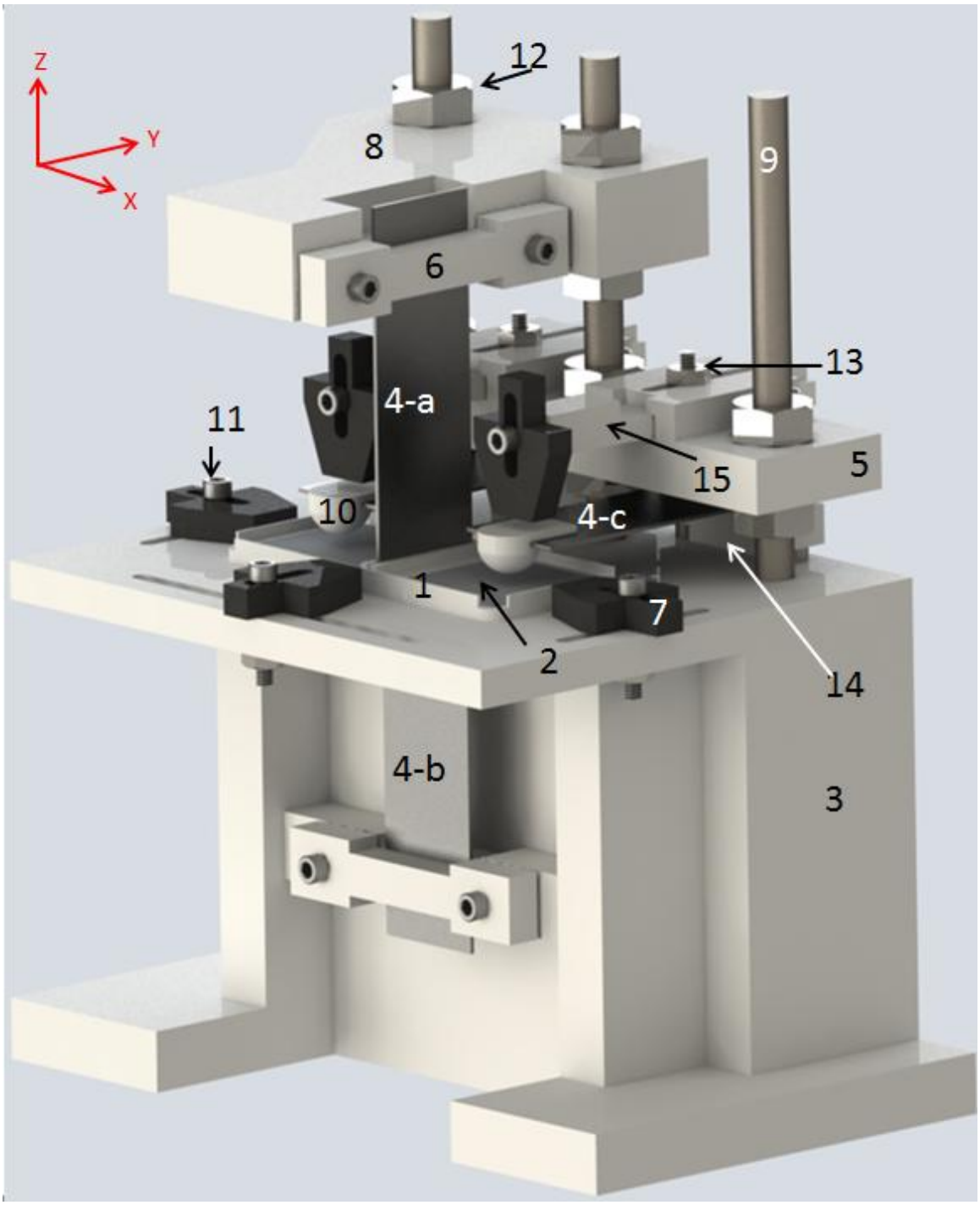


Fig. 2. SolidWorks rendering of final physical plant.

An overview of all system components, including those components labeled in the Physical Plant diagram can be found in *Appendix A. List of System Components*. Details regarding design and manufacture, as well as developing a system model are provided in Sections 2.2 and 2.3 on *Mechanical* and *Electrical Design and Development*.

## 2.2 Mechanical Design & Development

### 2.2.1 Developing a General Plant Model

The first design question answered pertained to the type of mechanism which can generate the desired positioning. Piezoelectric plate actuators, dubbed “bimorphs”, were chosen for their relatively low cost and high precision positioning. The bimorph operates on the piezoelectric principle that an applied voltage to a piezoelectric-type crystal will produce a geometric deformation. Two polarized piezoelectric ceramic strips are adhered to each other and given a ceramic coating as protection. The bimorph is cuboidal in shape with a very small thickness and a small aspect ratio. The piezoelectric crystals are polarized in the same direction and electrically connected in parallel. One end of the bimorph is mounted using a fixed support, while the other end is free. When electrical input is applied, one ceramic layer expands while the other contracts, resulting as a bending/flexing motion. In this project, the applied electrical signal has an alternating current, and therefore a cyclical bending motion, or vibration, occurs. The design utilized the tip displacement of the bimorph as applied to a mass, thereby doing work on that mass to achieve the desired vibration.

The Bimorph and its behaviors and mechanical aspects are discussed in detail in Sec. 2.2.2 *Optimal Selection of Bimorphs.*

To achieve three-degree-of-freedom positioning, two separate means were employed. The *Stage* was designed which would provide two-dimensional / planar vibration, by means of bimorphs, to the droplets deposited on it. One or more bimorphs could act in tandem for both the *X Direction* and the *Y direction* (See Fig. 2 and the corresponding component list, *Appendix A. List of System Components* for direction definitions). Because the *Stage* should vibrate in two dimensions independently, the bimorph-*Stage* interface needed to be dynamic and not static. The bimorph tip-in-slot method was chosen as a simple solution, involving slots built into the *Stage*. With the tip positioned with appropriate clearance inside a slot, the slot surface is able to slide back and forth across the bimorph tip surface perpendicularly to the pushing direction of the bimorph tip. This means that while the bimorph of a particular direction is vibrating the *Stage* in that direction, the bimorph of the orthogonal direction can also vibrate the *Stage*. Multiple bimorphs could also be incorporated, where each bimorph would have its own slot space.

In order to achieve motion in the third, vertical, dimension, the *Probe*, which contacts the droplet from above, was designed to be adhered near the tip of a horizontally opposed bimorph. The vibration of this bimorph would introduce vertical motion to the top of the droplet which is bridged between the silicon chip from below to the *Probe* tip above. Thus the droplet undergoing evaporation would be affected by vibration, in some form, with three degrees of freedom.

The driving mechanisms for motion of three degrees of freedom having been clarified, the next step was to develop a force model to describe the system behavior. The first model applies to the positioning *Stage*, and the second to the positioning *Probe*.

### *Dynamics Model of the Positioning Stage*

The goal of developing a dynamics model for the *Stage* in one-axis was to provide a baseline estimate on the critical limits for mass of the final system design. This model guided system design by quantifying both the upper threshold for the allowed mass and how this limit is both vibration amplitude- and frequency-dependent.

Eq. 1 shows the basic equation of motion as the foundation, focusing solely on one direction of motion, which is arbitrarily chosen as *X Direction* vibration. In theory, the collective bimorph force, less the developed friction, should equate to the displaced mass times acceleration. Although the target bimorph output waveform is triangular, the model assumes a sinusoidal waveform so that displacement can be differentiated to yield model acceleration.

$$n_x F_{bi,x} - f_{(bi-s),y} - f_{(s-b),x} = m\omega_x^2 A_x \sin(\omega_x t) \tag{1}$$

The list of equation components follows:

| | |
|---|---|
| $n_x$ | Number of acting bimorphs in *X Direction* |
| $F_{bi,x}$ | Individual force of *X Bimorph* |
| $f_{(bi-s),y}$ | Friction between the *Y Bimorph* and its *Stage* interface |
| $f_{(s-b),x}$ | Friction between the *Stage* and *Base* |

| | |
|---|---|
| $m$ | Total displaced mass |
| $\omega_x, A_x$ | Operating frequency and amplitude of the *X Direction* |
| $t$ | Time |

The basic friction formula is applied according to normal force and the coefficient of friction. Notice how the only bimorph-*Stage* interface friction which should impact the *X Direction* forces is that friction which results from the orthogonal, *Y Direction*, bimorphs with the *Stage*, hence the use of the subscript "y". For the *Y Bimorph-Stage* interface, the normal force is the net sum of forces acting in the *Y Direction*. The total frictional force provided by the *Y Bimorph-Stage* interface follows as Eq. 2.

$$f_{(bi-s),y} = \mu_{bi-s} m \omega_y^2 A_y \sin(\omega_y t) \tag{2}$$

Here, $\mu_{bi-s}$ represents the coefficient of friction for the *Y Bimorph-Stage* interface and $\omega_y$ and $A_y$ represent the *Y Direction* operating frequency and amplitude. As friction is independent of the surface area of interface contact, the number of acting *Y Bimorphs* is impertinent to the formula. Eq. 3 provides the frictional force for *Stage-Base* contact.

$$f_{(s-b),x} = \mu_{s-b} m g \tag{3}$$

Here, $\mu_{s-b}$ represents the coefficient of friction for *Stage-Base* contact and $g$ is the gravitational acceleration at earth's surface.

These results are substituted, resulting in Eq. 4

$$n_x F_{bi,x} - \mu_{bi-s} m\omega_y^2 A_y \sin(\omega_y t) - \mu_{s-b} mg = m\omega_x^2 A_x \sin(\omega_x t) \quad (4)$$

Focus then shifted to the individual bimorph applied force term, which has remained ambiguous previously. This required a focus on bimorph parameters. The two most important properties to be considered when evaluating piezoelectric actuator performances are the blocking force and free stroke deflection. The blocking force refers to the useable force the bimorph develops when deflection is blocked. In an alternate explanation, it is the force required to push back a fully energized actuator to zero displacement. The free stroke refers to the displacement achieved by the actuator at a given voltage level without the actuator working against any external load. Typically, as a subset of piezoelectric actuators, bimorphs exhibit large deflection ranges but small-scale blocking forces. Thus, mass and interface friction became critical factors for the *Stage* and interface design.

Fig. 3 represents the typical linear behavior between free stroke deflection and blocking force for a bimorph.

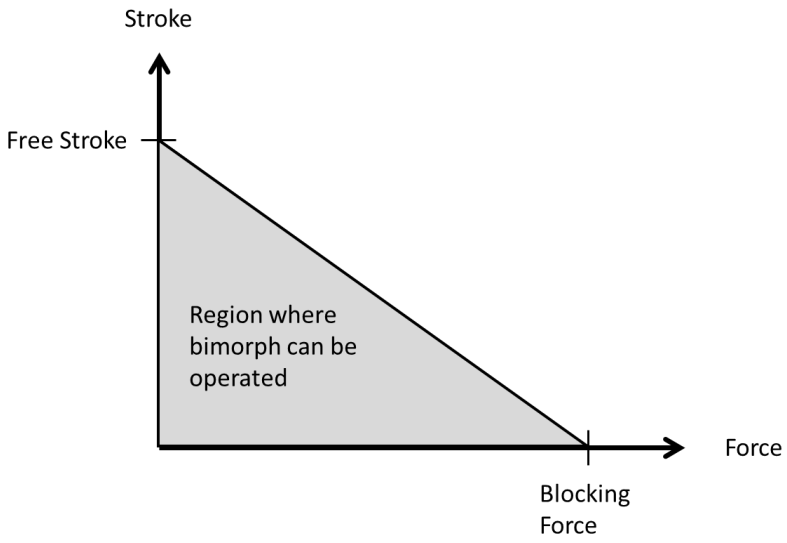


Fig. 3. Bimorph stroke versus force curve. Figure adapted from source [8].

Model assumptions are as follows:

1) The relationship between bimorph free stroke and blocking force is linear
2) Although there is a *region* of bimorph operation, free stroke and blocking force combinations are restricted to the outside boundary, representing the max possible pair values the bimorph can achieve.

Using the linear assumption, the bimorph force is solved and treated as the amplitude of a sinusoidal bimorph output, yielding Eq. 5.

$$F_{bi,x} = \frac{(A_{FS} - A_x)F_B}{A_{FS}} \sin(\omega_x t) = \left(1 - {}^{A_x}/_{A_{FS}}\right) F_B \sin(\omega_x t) \tag{5}$$

Here, $A_{FS}$ is the bimorph free stroke amplitude and $F_B$ is the bimorph blocking force. We assume the force is applied in a sinusoidal fashion through time, as with the previous model development. Substitution of Eq. 5 into Eq. 4 yields Eq. 6.

$$n_x \frac{(A_{FS} - A_x)F_B}{A_{FS}} \sin(\omega_x t) - \mu_{bi-s} m \omega_y^2 A_y \sin(\omega_y t) - \mu_{s-b} mg = m\omega_x^2 A_x \sin(\omega_x t) \quad (6)$$

Finally, the critical parameter, the total mass which the bimorph(s) displace in planar motion simultaneously, can be solved for. Eq. 7 results.

$$m = \frac{n_x (A_{FS} - A_x) F_B \sin(\omega_x t)}{A_{FS}\{\omega_x^2 A_x \sin(\omega_x t) + \mu_{bi-s}\omega_y^2 A_y \sin(\omega_y t) + \mu_{s-b} g\}}^{*} \quad (7)$$

$*$ This equation is limited for positive *X Direction* displacement only. Friction always opposes the direction of motion, and therefore the sign instantaneously flips for frictional forces when the direction of motion changes.

Since the design development is guided by the limiting mass quantity, the worst case scenario is evaluated to eliminate time from the equation and quantify this mass limit. Some general simplifications are also introduced.

The system was assumed symmetric with identical numbers of bimorphs acting per direction as well as identical operation amplitude and frequency for each direction. Thus the directional subscripts were dropped. It was also assumed that the coefficient of friction values are identical for each interface. This considers that each interface is lined

with the same, friction reducing, material, such as common Polytetrafluoroethylene (PTFE).

In the worst case scenario of forces, for simultaneous *X-Y Direction* motion, Eq. 7 is evaluated when each bimorph is at peak of the sinusoidal output. The mathematical equivalent is that each sinusoidal term, $\sin(\omega_x t)$ and $\sin(\omega_y t)$, has a magnitude of 1. This is the greatest magnitude the term can take on, and thus provides the worst case (or largest) force against which the bimorph has to recover in order to oscillate in the opposite direction.

Furthermore, at a peak or trough, the system is assumed instantaneously static, and thus the *static* coefficient of friction values are used, which are also the worst case over dynamic values. The interface friction values are now amended with a subscript to denote this and these worst case scenario simplifications yield Eq. 8.

$$m = \frac{n\left(1 - {A}/{A_{FS}}\right)F_B}{\omega^2 A(1+\mu_S) + \mu_S g} \tag{8}$$

***Dynamics Model of the Positioning Probe***

The motion model for the *Z Direction* follows the same basic outline as for the planar motion model. Again, we start with a force analysis. The sum of forces in the *Z Direction* must overcome the mass and its acceleration as in Eq. 9.

$$F_{bi,z} - mg = m\,\mathrm{A}_z\omega_z^2\sin(\omega_z t) \tag{9}$$

The bimorph force is derived in the same way as is shown in Eq.5, with subscripts being the only difference. Eq. 10 results.

$$F_{bi,z} = \frac{(A_{FS} - A_z)F_B}{A_{FS}}\sin(\omega_z t) \tag{10}$$

Again, sinusoidal output is assumed. Substitution and rearranging yields the final time dependent mass limitation model, Eq. 11.

$$m = \frac{(A_{FS} - A_z)F_B\sin(\omega_z t)}{A_{FS}\{\omega_z^2 A_z\sin(\omega_z t) + g\}} \tag{11}$$

An important difference between this *Z Direction* model and the *X-Y Direction* model is the independency of vibration in different directions. As described previously, the bimorphs for *X-Y Direction* motion act on the same mass, and therefore are consequently coupled together. The *Z Bimorph*, however, acts completely independently since its target mass to vibrate is the *Probe*, and there are no other degrees of motion tied to the *Probe*.

Another difference to note is the absence of friction. Again this is consequential of the independency of Z motion. For all model cases, air resistance (friction) is neglected as a simplifying measure.

A similar worst case scenario analysis is taken. Since the force balance assumes the bimorph is at the bottom of the sinusoid wave and gravity is working against the bimorph effort, the sinusoidal terms take on magnitude 1. In general, the trough and peak

of motion are not equivalent scenarios since the system forces are asymmetric. The mass the system is able to handle at the trough is more limited than at the peak due to the constant downward acting gravitational force. Mass-limiting Eq. 12 results.

$$m = \frac{(A_{FS} - A_z)F_B}{A_{FS}\{\omega_z^2 A_z + g\}} \tag{12}$$

### 2.2.2 Optimal Selection of Bimorphs

The effects of bimorph parameters on limiting the allowed mass were analyzed in a Microsoft Excel document shown as Table 1.

| Parameter | | Symbol | Units | Given Values | Secondary Calculation |
|---|---|---|---|---|---|
| DESIGN VARIABLES | | | | | |
| Amplitude of vibration displacement | | A | [μm] | 500 | |
| frequency of vibration | | f | [Hz] | 25 | |
| angular velocity (frequency) | | ω | [rad/sec] | | 157.0796327 |
| Bimorph Blocking Force | | | | | |
| | APC 40-2010 | $F_{bi}$ | [N] | 0.420 | |
| | APC 40-2020 | $F_{Bi}$ | [N] | 0.716 | |
| | APC 40-2030 | $F_{Bi}$ | [N] | 0.064 | |
| | | | | | |
| Bimorph Free Stroke | APC 40-2010 | $A_{FS}$ | [m] | 6.31E-04 | |
| | APC 40-2020 | $A_{FS}$ | [m] | 2.13E-04 | |
| | APC 40-2030 | $A_{FS}$ | [m] | 2.46E-04 | |
| FIXED CONSTRAINTS | | | | | |
| number of contributing bimorphs IN X | | $n_X$ | [] | 1 | |
| number of contributing bimorphs IN Y | | $n_Y$ | [] | 1 | |
| number of contributing bimorphs IN Z | | $n_Z$ | [] | 1 | |
| MATERIAL SELECTION | | | | | |
| Density of Stage / Probe | Porous Al Alloy | ρ | [kg/m$^3$] | 1799 | |
| | ABS Plastic | ρ | [kg/m$^3$] | 1052 | |
| | LDPE | ρ | [kg/m$^3$] | 913 | |
| Density of Wafer | Silicon | $\rho_W$ | [kg/m$^3$] | 1215.15 | |
| Volume of wafer | Silicon | $\forall_W$ | [m$^3$] | 9.6774E-07 | |
| Mass of Wafer | Silicon | $m_W$ | [kg] | | 1.18E-03 |
| Density of droplet | Water | $\rho_D$ | [kg/m$^3$] | 28.32 | |
| Volume of droplet | Water | $\forall_D$ | [m$^3$] | 1.00E-08 | |
| Mass of droplet | Water | $m_D$ | [kg] | | 2.83E-07 |
| PTFE Tape Coefficient of Friction, STATIC | | $\mu_S$ | [] | 0.2 | |
| ABS Coefficient of Friction, STATIC | | $\mu_S$ | [] | 0.6 | |
| OTHER | | | | | |
| Acceleration of gravity | | g | [m/s$^2$] | 9.81 | |

Table 1. Excel documented created to aid bimorph optimization.

Input parameters to the document included *Stage/Probe*, droplet, and *Silicon Chip* density. Droplet density was estimated to be that of pure water. Three different *Stage/Probe* densities were input based on three example manufacture materials. A typical coefficient of static friction value was used for PTFE.

After careful research of companies offering piezoelectric actuators, the actuator choice was narrowed to three final bimorphs offered by the American Piezo Company (APC). These bimorphs fall under design variables since the final bimorph selection is a design choice. The blocking force and free deflection of each bimorph are fixed properties given by the manufacturer. The number of acting bimorphs per direction was limited to one bimorph due to limitations on the number of amplifier channels available to drive the bimorphs.

The document outputs the max allowable mass of the *Stage* according to bimorph and *Stage* material and amplitude and frequency definition. It can be seen from the document that no analyzed bimorph produces a free deflection equal to or in excess of one millimeter. This dictates that despite the target maximum amplitude of vibratoin, 1 millimeter of half-deflection cannot be achieved. Thus, the maximum operating amplitude was constrained to be below the free deflection.

While frequency was kept constant, the amplitude limit was adjusted to yield a reasonable volume limit which could be achieved through design and manufacture. Initial iterations of *Stage* design showed that a volume at least as low as 2.5 cubic centimeters could be accomplished. Table 2 shows the results for the three bimorph options and three *Stage* materials.

| Bimorph | Total Mass Limit [g] | | Component Mass Limit [g] | | Stage / Probe Material | Component Volume Limit [$cm^3$] | |
|---|---|---|---|---|---|---|---|
| | *X - Y Direction* | *Z Direction* | $m_{Stage}$ | $m_{Probe}$ | | $V_{Stage}$ | $V_{Probe}$ |
| APC 40-2010 | 5.20 | 3.94 | 2.85 | 3.94 | Porous Al Alloy | 1.58 | 2.19 |
| | | | | | ABS Plastic | 2.71 | 3.74 |
| | | | | | LDPE | 3.12 | 4.31 |
| APC 40-2020 | -57.58 | -43.59 | -59.93 | -43.59 | Porous Al Alloy | -33.31 | -24.23 |
| | | | | | ABS Plastic | -56.97 | -41.44 |
| | | | | | LDPE | -65.64 | -47.74 |
| APC 40-2030 | -3.96 | -3.00 | -6.31 | -3.00 | Porous Al Alloy | -3.51 | -1.67 |
| | | | | | ABS Plastic | -6.00 | -2.85 |
| | | | | | LDPE | -6.91 | -3.28 |

Table 2. Optimal bimorph selection for both the *Stage* and *Probe* Based on a trajectory of 25 Hz and 500 $\mu$m.

Equations 8 and 12 were used to determine the total mass limit for the *X-Y Direction* and the *Z Direction*, respectively. The mass of the *Stage* was determined by subtracting the approximated mass of two DNA solution droplets and two silicon wafters from the total mass figure. The reason for a pair of wafer-droplet's was to maintain symmetry in the final *Stage* design, as is described in Sec. 2.2.3 *Stage Design and Manufacture*. The mass of the *Probe* was determined directly from the Total Mass Limit since the *Probe* carries no extra mass. Three final allowed *Stage* and *Probe* volume figures result for each bimorph choice due to three possible material (density) choices. The first choice is a porous aluminum alloy, offered for raw material sale from the company McMaster Carr. This material candidate reflects the manual machining option. The second choice is Acrylonitrile Butadiene Styrene (ABS) plastic. This material candidate reflects the automated (Rapid Prototyping) machining option. The third choice is low-density polyethylene (LDPE) plastic, offered for raw material sale from the company McMaster Carr. This candidate also reflects the manual machining option.

As seen in the figure, the APC catalogue number 40-2010 bimorph is the best choice as it allows the only positive mass limitation across the range of candidate *Stage/Probe* materials. Although LDPE was the lowest density material with which to make the *Stage/Probe*, ABS was chosen as the final material. This is because the Rutgers Mechanical Engineering department has in-house rapid prototyping which was free of charge. Choosing rapid prototyping with ABS plastic saved both time and money, as the other options required both purchase of material and manual machining effort.

### 2.2.3 *Stage* Design & Manufacture

***Design***

In order to complete the first design step of building a system model, some aspects of *Stage* design had to be predetermined. For example, the *Stage* should allow space for a silicon wafer, on which would be deposited the DNA solution droplet for experimentation. The method of interface between the driving mechanism (bimorph) and *Stage* was a critical predetermined factor. It was discussed that any given interface must serve two functions:

1) Allow the bimorph of the current interface to apply a force to displace the *Stage* in the horizontal plane.
2) Allow the *Stage* to be displaced by a separate bimorph of a separate interface in an orthogonal direction, still within the horizontal plane, and without interference from the current interface.

More importantly still, the interface must serve these two functions *simultaneously* and *independently*. The devised solution is referred to as the tip-in-slot method. The *Stage* was designed such that the actuating tip of the bimorph would fit into a slot on the *Stage*. The walls of the slot would then "sandwich" the tip of the bimorph, thus allowing the bimorph a platform through which to apply a force to displace the *Stage* back and forth along one direction of motion. To achieve total planar motion, the *Stage* would need two slots oriented perpendicular to each other. If the proper slot width is designed, this method also allows the slot walls to slide back and forth along the bimorph tip for motion in the orthogonal direction. Careful consideration of slot width was paramount. If the slot width is less than or equal to bimorph tip width, a compression force is added to the normal force term of $f_{(b-s),y}$ in the evaluation of *X Direction* sum of forces. The narrower this width, the more devastating the compression force, and therefore friction, becomes. There is a threshold where the *Y Bimorph* would no longer be capable of displacing the bimorph. The same goes for a force analysis of the *Y Direction*.

Another problem scenario is for a slot width too large. This scenario would result in a pure time delay system. Time delays are a common phenomenon in many engineering systems; however they can provide instability and poor performance for such systems [9]. Considering the tip of the bimorph in the slot, the tip has to traverse a certain amount of empty gap space before the *Stage* even begins to move. Also, at the peak or trough of the waveform, there is an undesirable impact where the back wall of the slot "rams" into the bimorph as it changes direction. Consequent to this behavior are undesirable vibrations and dynamics.

Another predetermined aspect of *Stage* design was the number of acting bimorphs. Due to limitations in hardware such as the number of output channels for both the amplifier and data acquisition card allotted for this research project, the number of bimorphs to drive the *Stage* was limited to one per direction. Early iterations and plant prototypes involved more than one bimorph per direction by simply using one amplifier channel per direction and running multiple bimorphs off the same channel. Two problems arose. There is a limiting factor since each bimorph draws its own power from a constant amplifier power source. Also, each bimorph does not display quite identical behavior. For two bimorphs which are supposed to operate in unison to position in one direction, different behaviors can induce undesired vibrations and/or twisting motions of the *Stage*.

Considering these aspects, after many iterations of *Stage* design, the final *Stage* design is represented in Fig.'s 4, 5, and 6.

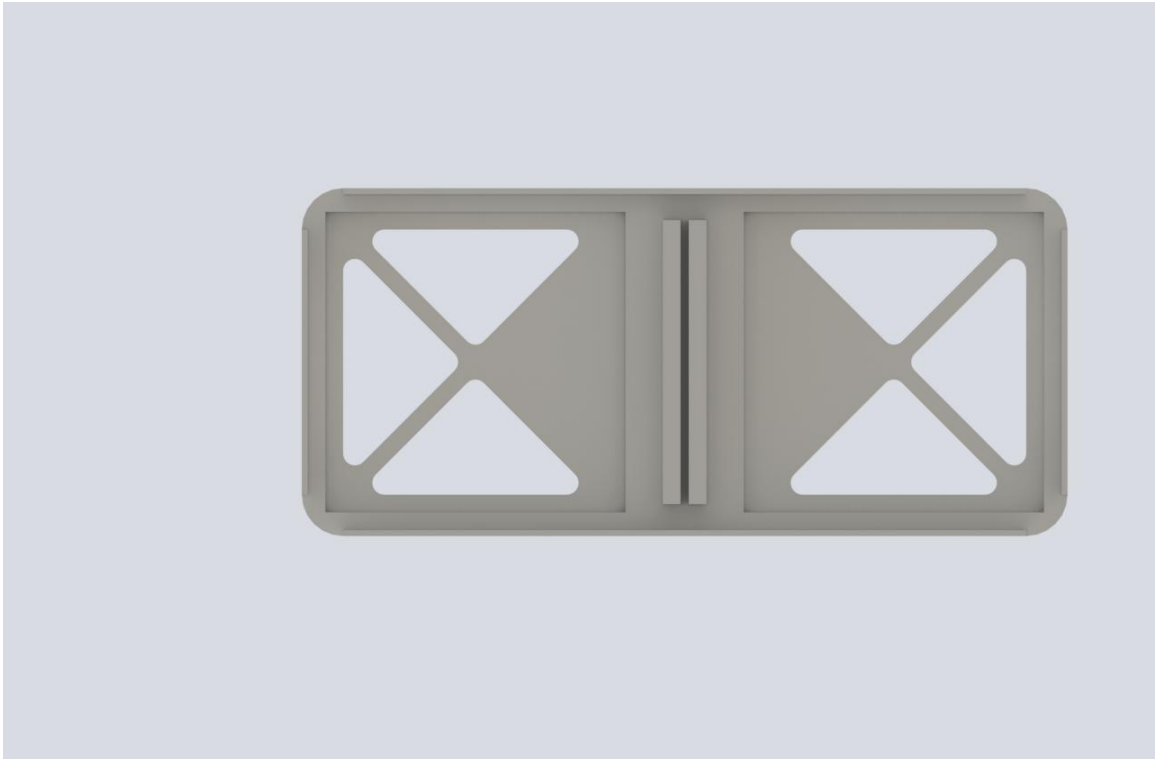

Fig. 4. *Stage* top view.

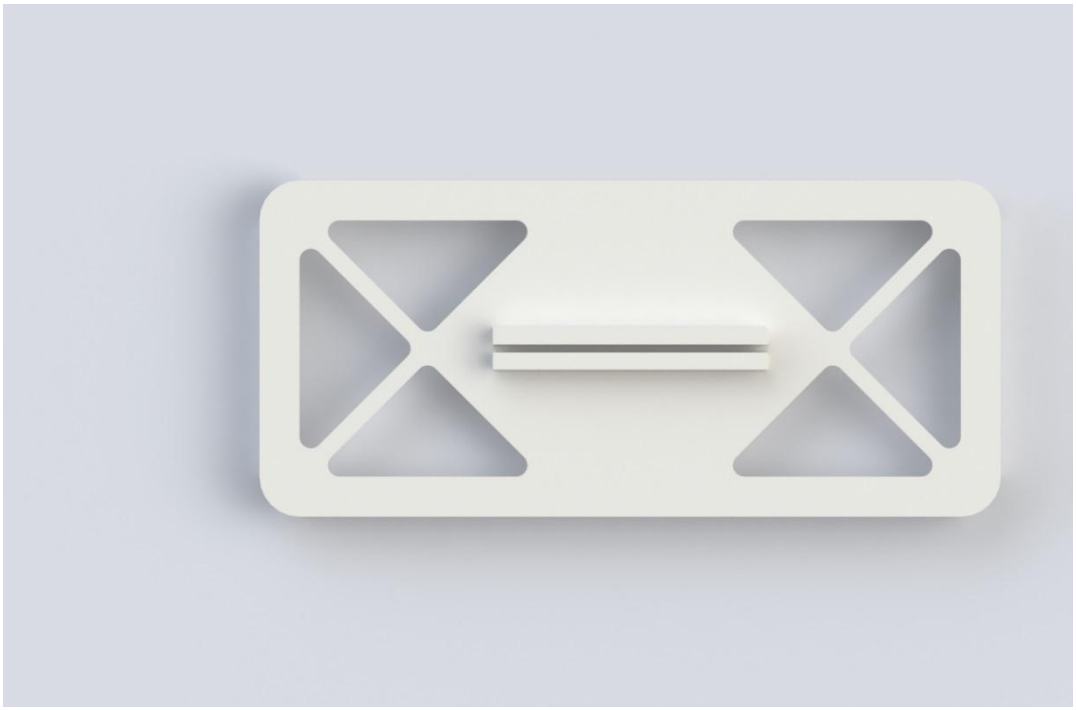

Fig. 5. *Stage* bottom view.

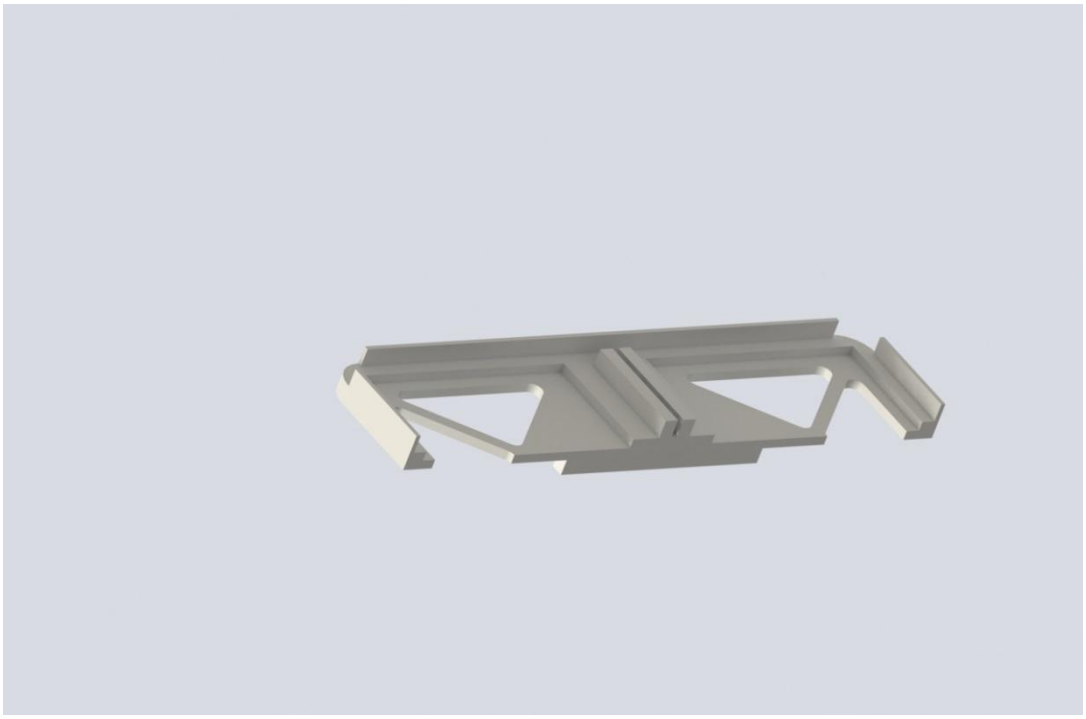

Fig. 6. *Stage* cut-section view.

The three views show several features of the final *Stage* design:

1) Two Square cut-outs on the top side for fitting two separate silicon wafers for the purpose of hosting two droplet evaporations
2) Thin walls extruded from the top of all four sides providing a wide enough surface to be sensed by sensors located anywhere along all four sides
3) Two slots for hosting bimorph tips, oriented perpendicular to each other and positioned symmetrically at the center of both the top and bottom of the *Stage*.
4) Triangular cut-outs to reduce *Stage* mass.

A critical feature developed through *Stage* iterations was the particular placement of the slots for bimorph interfacing. If the slots were positioned on the outer edges of two adjacent and perpendicular sides of the *Stage*, there could arise a resulting net moment on

the *Stage* due to the bimorph-*Stage* friction term. This is because this configuration gives rise to a lever-arm distance between the *Stage* center of mass and the line of action of the opposing friction force. Earlier iterations provided multiple bimorphs per direction of motion, with an even number of bimorphs being placed on each side of the *Stage*. Thus, the resulting moments would cancel. However, due to the single bimorph limitation, there will arise a net moment. This has been shown in prototypes/earlier iterations to cause a non-negligible "twisting" of the *Stage* during motion, a highly undesirable characteristic.

With the slot placement as shown, the friction force term acts along a line which passes directly through the *Stage* center of mass, thus resulting in a zero net moment. However, this assumes a symmetric *Stage*. Since the experimental wafer-droplet pair can no longer be placed at the center of the *Stage* area, as it were in previous iterations, it must be placed off-center. In order to maintain symmetry, two silicon chips and droplets are used, on pair on each side of the *Stage* center. This has the added bonus of allowing the user to conduct two evaporation experiments simultaneously.

The placement of slots itself predetermines the location of the acting bimorphs. Since the slots would interfere and intersect when at the same vertical height, they are placed on the top and bottom of the *Stage*. Due to this, the bimorphs must also be located on two different sides of the *Stage*. One bimorph interfaces from the top and, by arbitrary convention, displaces the *Stage* in the *X Direction*. The other bimorph interfaces from the bottom and displaced the *Stage* in the *Y Direction*. The overall *Stage*, bimorph interfacing system is represented in Fig. 7.

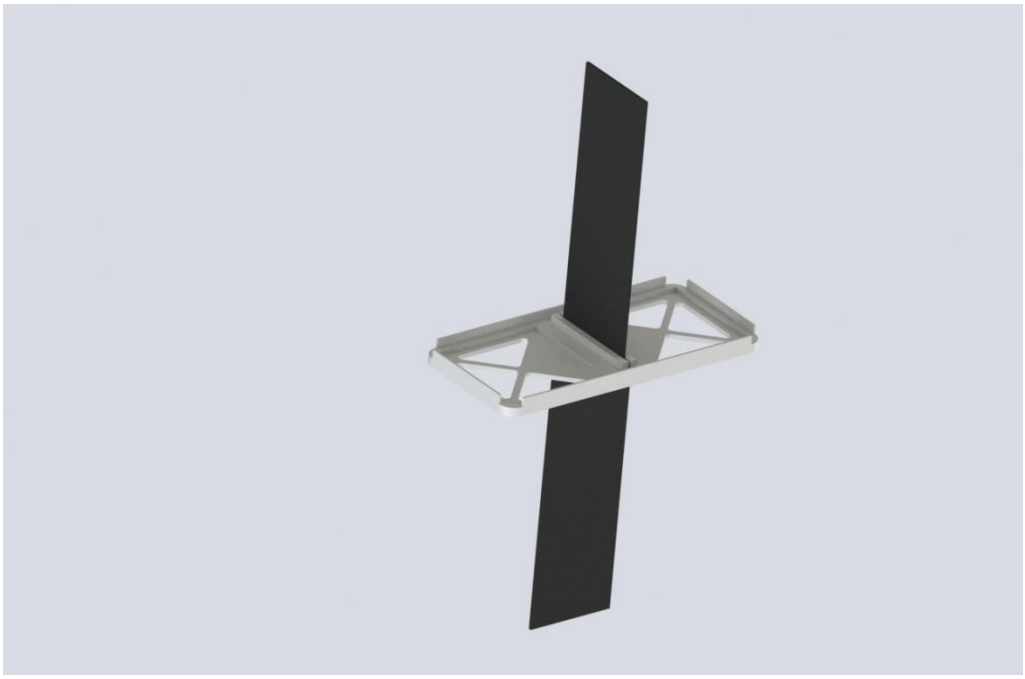

Fig. 7. Interfacing between the *Stage* and *X* and *Y Bimorphs.*

The output limiting volume figure guided multiple iterations of CAD *Stage* design. SolidWorks CAD software was used with the *measure* function to quantify model volume. The final *Stage* volume was virtually measured at 2.35 cubic centimeters, representing approximately 87% of the critical, or maximum allowed, *Stage* volume. This represents the achieved safety factor, though minor, for *Stage* volume. This was due to the many simplifications and estimates that were assumed in the development of the plant model. For example, there was no guarantee that such a low coefficient of friction can be achieved, depending on if and how PTFE could be effectively applied. A significant simplification was using a sinusoidal wave model for development of the equation of motion. As the target wave is a triangle wave, there is significantly larger acceleration with a greater force against the bimorph at the wave peak and troughs during operation. This also increases the normal forces quantified for the friction calculations.

***Manufacture***

As discussed previously, automated machining called Rapid Prototyping was the chosen manufacture method for the *Stage*. The machine used was a department owned and operated Stratasys Inc. U Print SE. This machined printed using a technology called Fused Deposition Modeling (FDM). As was part of the attraction, the printing and material was free of cost.

There were included several post-machining manufacture processes as well. The outer face of each vertical sensor-target wall on all four sides of the *Stage* was fitted with a strip of white paper. Double sided scotch tape was used to adhere the white printer paper strips. These white paper strips provided the proper reflecting surface for sensor operation, as discussed in Sec. 2.3.2 *Sensing System Design.*

The bimorph-*Stage* interface slots were ultimately machined with a gap equivalent to the bimorph thickness. The post machining process included using a small-grit sandpaper to widen this gap and test the setup at a given gap width, repeating this process until the gap width offered a reduced friction but no user-visible space between the bimorph and slot wall.

### 2.2.4 Silicon Wafer Manufacture

A square shaped cut of silicon was chosen to provide a smooth and inert platform on which the experiment with the DNA solution droplet can take place. Manufacture and

cutting of two silicon chips to the one square-inch size desired to fit the *Stage* was outsourced to a different department, as per the suggestion of the project advisor.

### 2.2.5 *Probe* Design & Manufacture

#### *Design*

*Probe* design considerations follow naturally from derivation of the dynamics model for *Probe* positioning. Only one *Z Bimorph* is responsible for inducing vibration in the *Z Direction* on a single mass, the *Probe*. Inherent from the *Stage* design, this gives the plant a total capacity of 2 bimorphs for the *Z Direction*, or one for each of two experiments it is possible to conduct simultaneously.

As seen before, the interface between the bimorph and the mass to vibrate is an important design consideration. In the case of Z vibration, the problem is a much simpler one. Since there is only one degree of freedom tied to the *Probe* mass, the interface between the *Probe* and *Z Bimorph* is allowed to be rigid. This eliminates a need to worry about friction forces from a dynamic interface as well as time delay uncertainties derived from the gaps between bimorph and mass surfaces at the interface.

Another design consideration is the geometry of the *Probe*. Recall from earlier that the droplet is deposited on the *Silicon Wafer* and the *Probe* is lowered to make contact with the top of the droplet, allowing the droplet to create a “bridge” between the silicon surface and the *Probe*. As per studied literature, it is common for the contact region of the *Probe* to be spherical, and therefore the *Base*line design for this project is a spherical *Probe* contact surface. Fig. 8 shows the final Baseline *Probe* design as interfaced with a *Z Bimorph*.

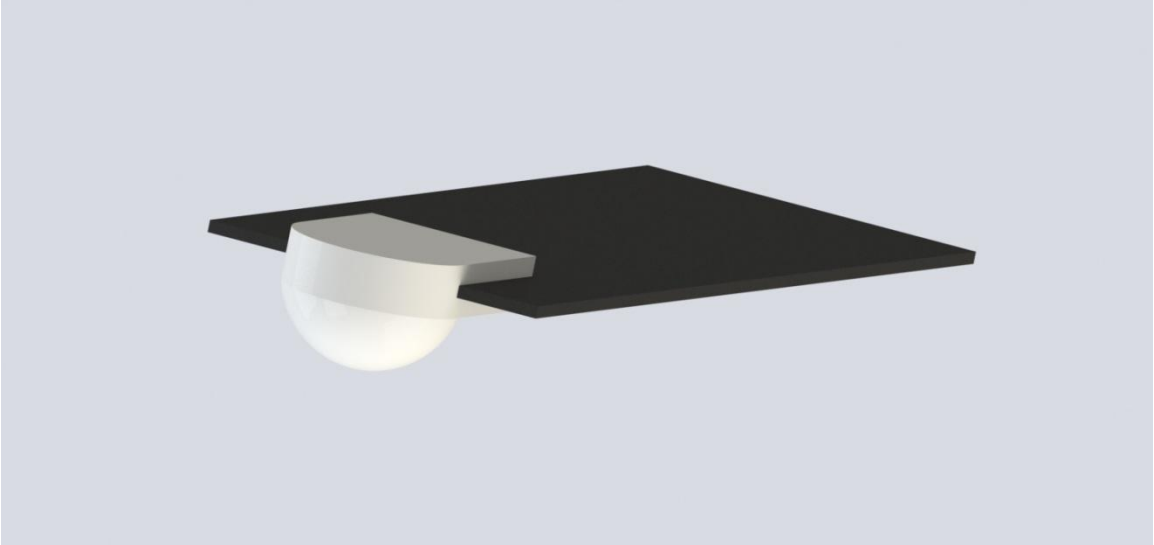

Fig. 8. Sub-assembly of a *Probe* and *Z Bimorph.*

The interface design between the *Probe* and bimorph is a slot. The slot is machined to a width sufficiently smaller than the bimorph thickness such that the *Probe* will remain stationary on the vibrating bimorph tip yet the interface is not too narrow for bimorph mounting. For this project it has been termed a "pre-load fit". This interface was a rather simple design which reduced the need for hardware and frivolous additional *Probe* mass. The pre-load fit also eliminates the need for a *Probe*-to-bimorph adhesion substance, thereby allowing the *Probe* to be interchanged with one of a different geometry without the need to change the bimorph as well. In this way, the *Probe* was designed to be cost effective.

The *Probe* was also designed with a flat surface of sufficient area to provide a sensing surface for the reflective object sensor. As seen in the figure, the top of the *Probe* structure is flat and provides an area on which the proper material can be adhered for purposes of sensing displacement.

***Manufacture***

The *Probe* was a proof of concept design and not physically manufactured. The critical post machining process for the *Probe* is adhering a strip of white paper to the top surface of the *Probe* using double sided scotch tape. These white paper strips provided the proper reflecting surface for sensor operation, as is discussed in Sec. 2.3.2 *Sensing System Design.*

### 2.2.6 *Base* Design & Manufacture

***Design***

After determining the subsystems to provide motion in the *X*, *Y*, and *Z* Directions, the next design question involved the method of containing / mounting these subsystems and their required sensory systems. Thus the logical next design was that of the *Base* structure. A list of features was devised which the *Base* design was required to accommodate for:

1. A flat X-Y plane platform on which the *Stage* can undergo planar vibration
2. A mounting system for each system bimorph (*X*, *Y*, and two *Z Bimorph*s) to be contained with the correct orientation.
3. The *Z Bimorph* vertical mounting height should be adjustable in order to place the attached *Probe* correctly.

4. A sensor mounting system so that all three directions of motion, X and Y with the *Stage* and Z with the *Probe*, can be quantified
5. Room allowed for coating of surface with PTFE tape

After several design iterations using the CAD software SolidWorks, Fig. 9 below shows a rendering of the final *Base* design.

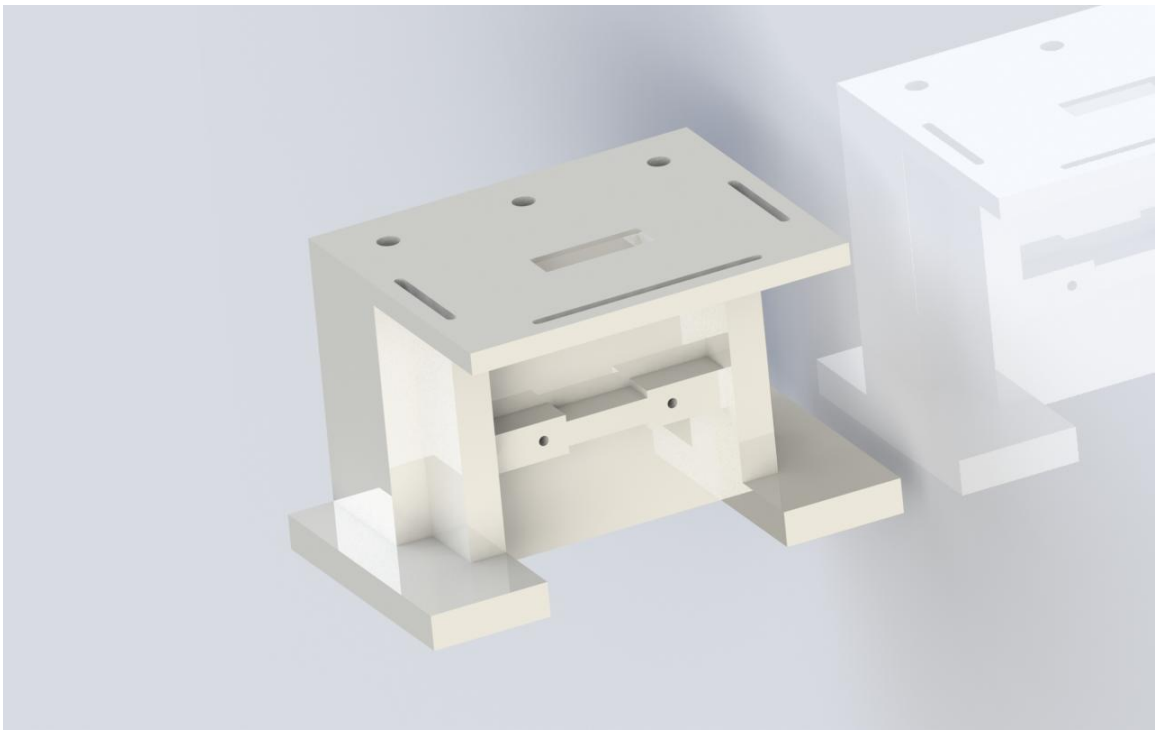

Fig. 9. Final *Base* design.

The design provides a flat platform surface on top, on which the *Stage* is able to vibrate in planar motion.

Near center on the platform surface is a square cut which allows the *Y Bimorph* to mate with its corresponding slot on the bottom of face of the *Stage* from below. The cut was designed large enough so that the *Y Bimorph*'s tip – *Stage* slot mate would not interfere with the walls of the cut during vibration.

The *Stage* is centered over top of the cut. Considering a virtual rectangle of area which encompasses the *Stage* as well as all possible platform space the *Stage* could occupy during motion, other features of the *Base*'s platform were designed not to interfere with this space. Slots were designed along three sides of this virtual rectangle with a small distance from the rectangle. These slots provide the mounting system for the planar reflective object sensors. The sensors themselves have a longitudinal slot. This design allows a sensor to be mounted with the sensor slot oriented perpendicular to the *Base* platform slot. The sensor is mounted in place using a socket head cap screw and corresponding hex nut. Using the *Base* slot, a sensor can be moved side to side in order to target a particular section of a *Stage* sensing face. Using the sensor slot, a sensor can be moved forward and backward to alter the sensing distance between the sensor face and *Stage* sensing face. This design hands the user complete control for sensing the planar vibration of the physical plant.

The rear of the *Base* platform hosts three tapped hole features, evenly spaced, which accept a total of three threaded rods. This feature provides the mechanism through which the *X Bimorph*, *Z Bimorph*/*Probe* assemblies and corresponding *Z Direction* sensors are mounted. Two mounts, one for the *X Direction* bimorph and one for the *Z Bimorph*s and sensors, are designed with corresponding through-holes. These mounts can slide onto the threaded rods and are held in place by the rods corresponding hex nuts from above and below each through hole. Design and manufacture are detailed for each mount in their separate document sections.

Below the platform is a hollow area where the *Y Bimorph* can be mounted in a vertical fashion. An extruded section provides the means to mount the *Y Bimorph*

directly to the *Base*. The extruded section width varies, with a smaller width where the bimorph is centrally mounted and larger widths to each side of the center where the socket head cap screws of the clamping mechanism get screwed into the *Base*. The smaller thickness is designed to provide a stable surface area for clamping the bimorph without constraining too much surface area of the overall bimorph. The face of the extrusion which accepts the screws has a larger thickness so as to reduce the stress concentration at the screw-hole and reduce the probability of crack formation between the hole face and top/bottom faces of the extrusion.

Along the bottom of the *Base* there is an outcrop/ledge around three sides of the *Base*. This ledge provides material through which, if need be, holes can be drilled in order to mount the overall *Base* to a sub-Base with bolts. This would increase the amount of mass the *Base* has and therefore decrease susceptibility to unwanted vibrational effects from the vibrating bimorphs through the *Base* structure.

***Manufacture***

The *Base* underwent both automated and manual machining processes. The *Base* model was split into two models in the CAD phase. One model did not include any hole features of the *Base* but did include the slot features. This model was used for rapid prototyping purposes. As previously mentioned, rapid prototyping was a readily available and financially optimal machining method for this project.

The second model included all *Base* holes and was used as a user reference for the manual machining process. A milling machine was used to drill and tap the three ¼" - 20 holes on the *Base* top and two 4 – 40 holes along the *Base* front for bimorph mounting.

The post machining process involved layering two strips of PTFE tape, one along each long-side of the *Base* platform rectangle cut. This PTFE tape was the actual surface the *Stage* would vibrate on and provided the low coefficient of friction estimate included in the system model formulations.

### 2.2.7 *X Mount* Design & Manufacture

#### *Design*

The *X Mount* refers to the mechanism which mounts and holds in place the *X Bimorph.* This direction is defined as parallel to the short sides of the *Stage*. Fig. 10 provides a SolidWorks rendering of the final *X Mount* design.

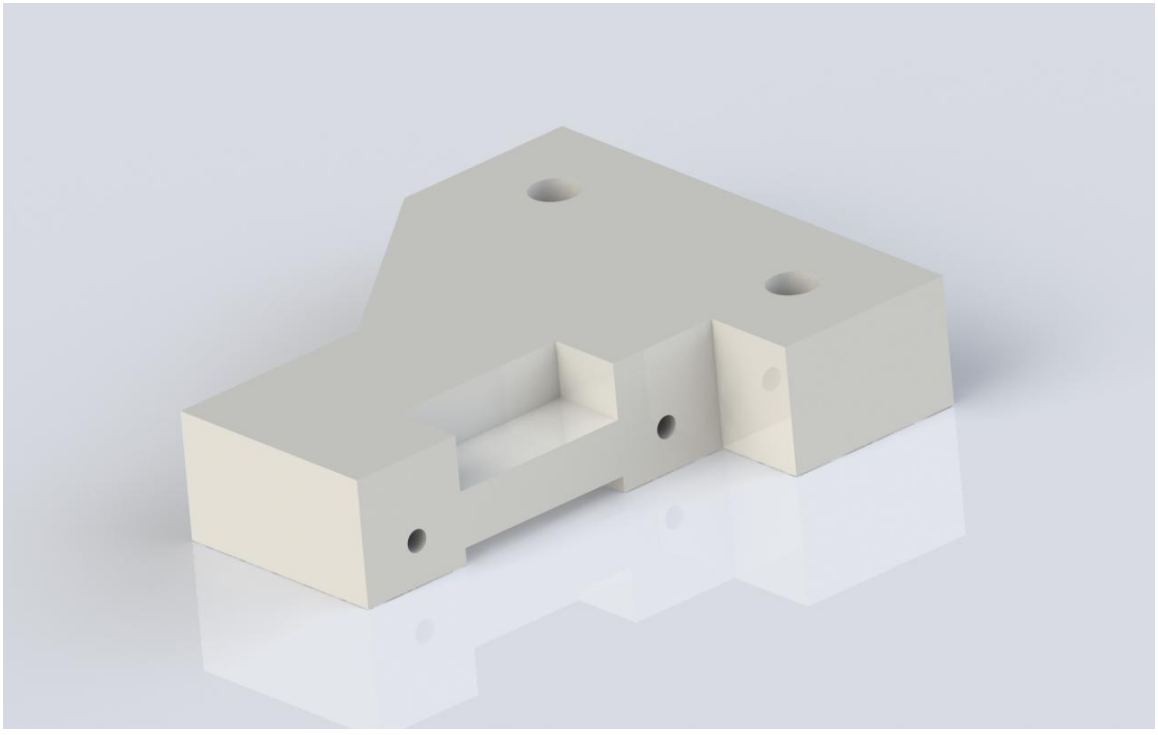

Fig. 10. Final *X Mount* design.

As discussed in the *Base* design section, two through-holes are designed into this mount which matches the outer diameter of the threaded rod. This is so that this mount can slide over two of the three rods threaded into the *Base* piece. It was arbitrarily chosen that the piece be designed to slide over the left and center threaded rod extending from the *Base*, when viewing the *Base* from the front.

This mount is designed at 16 millimeters thick to provide a rigid-enough support the vibrating *X Bimorph* without taking up too much space. Similar to the extruded section for mounting the *Y Bimorph* to the *Base,* an extruded section provides a smaller width platform for mounting the bimorph and a larger width platform where the holes are drilled to reduce the stress concentration. As with the *Y Bimorph* mounted to the *Base,* the *X, Y Bimorph Clamp* was used to mount the *X Bimorph* to the *X Mount* using socket head cap screw hardware as shown in the following Fig. 11.

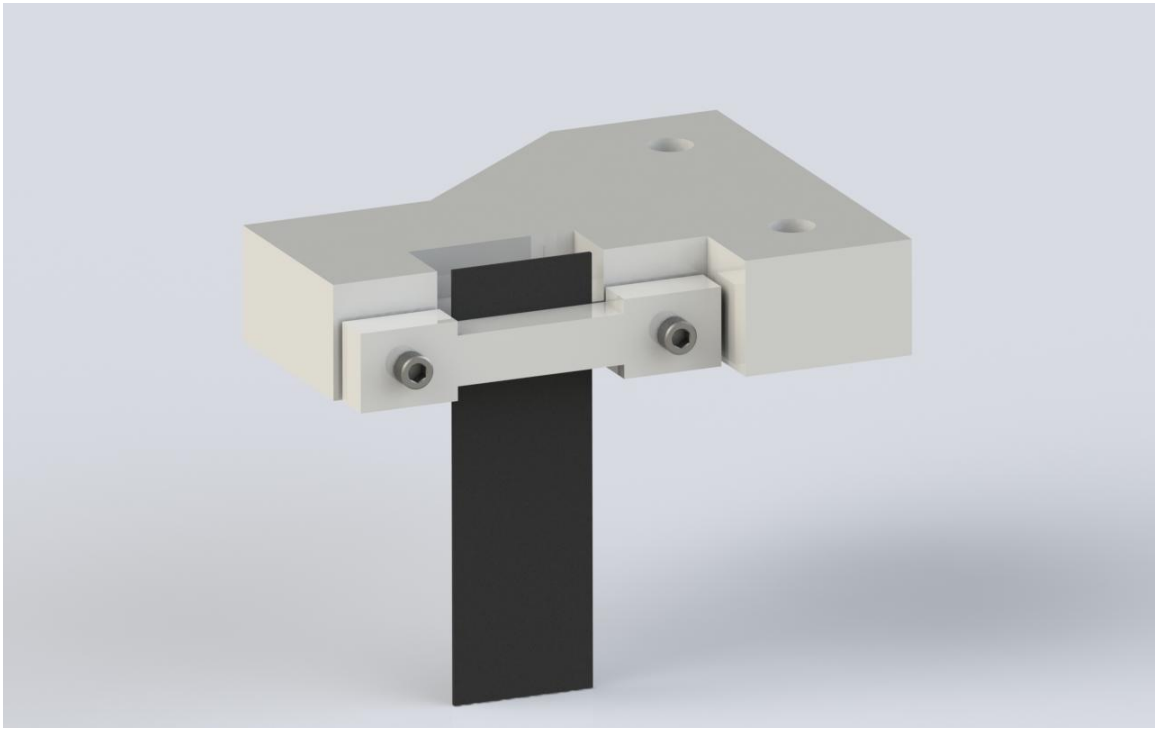

Fig. 11. Rendering of *X Mount* with mounted *X Bimorph.*

***Manufacture***

The *X Mount* was machined using a combination of automated and manual methods. The overall structure was machined using Rapid Prototyping. The two top surface through-holes were manually drilled on the mill and the bimorph mount holes were both drilled and tapped.

### 2.2.8 *Z Mount* & *Z Sensor Rail* Design & Manufacture

***Design***

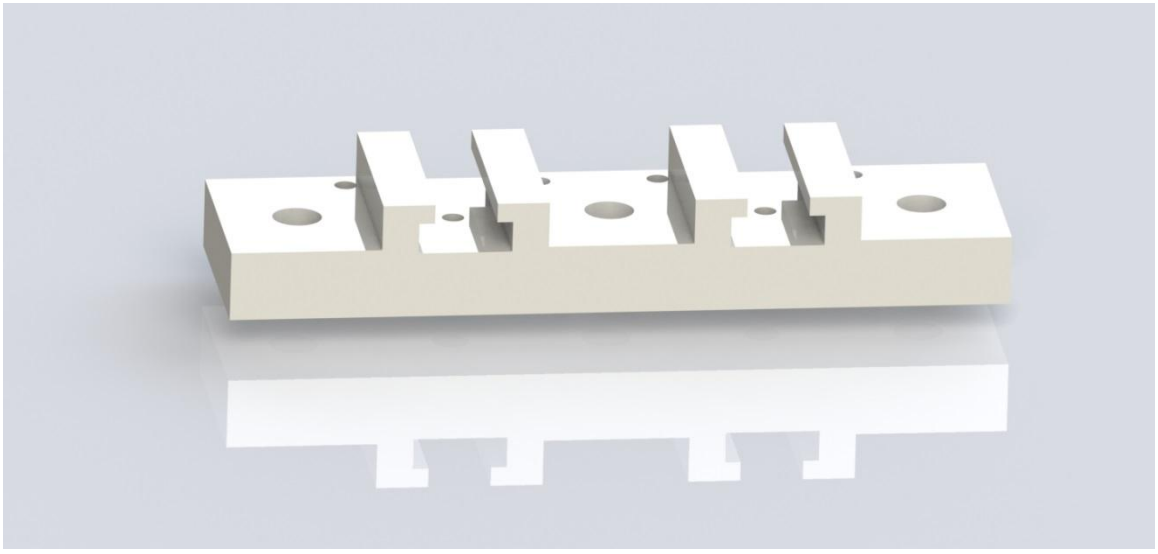

Fig. 12. Top-Front View of *Z Mount.*

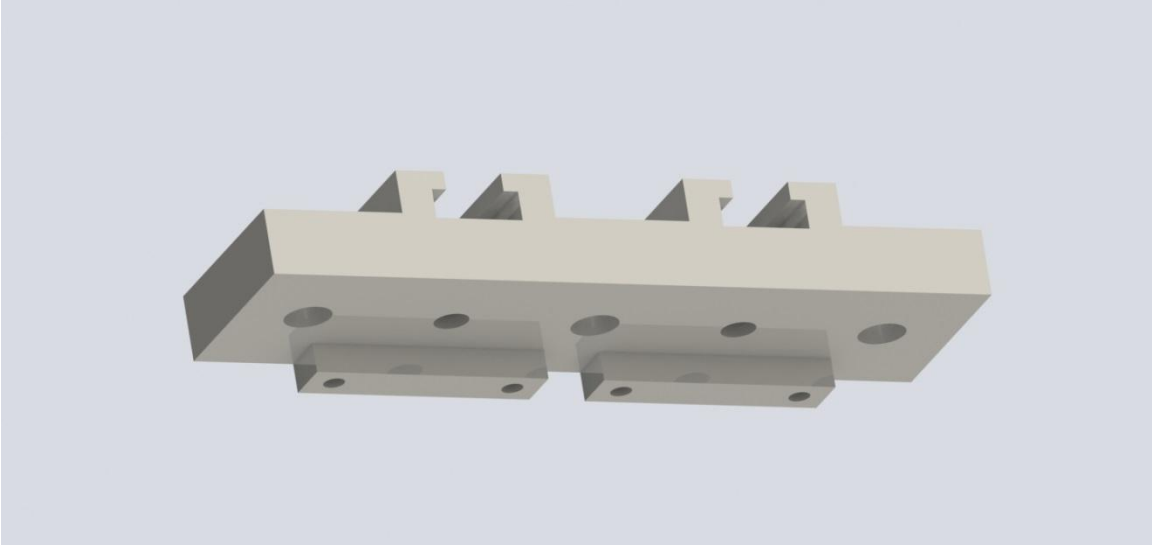

Fig. 13. Bottom-Front View of *Z Mount.*

Figures 12 and 13 show partial top and bottom views of the *Z Mount* with a viewing perspective from the front of the piece. The front of the piece is the side of the piece where the reflective object sensors are mounted and where the bimorph free tips are vibrating. From these views several features can be outlined.

On the bottom surface of the mount, two raised platforms are designed at the rear of the mount, each with a pair of drilled and tapped holes. Each of two *Z Bimorphs* is mounted at these platforms, being held in place by the accompanying *Z Clamp* pieces and a pair of socket head cap screws. The screws thread straight into the holes since the holes are tapped.

Three main quarter inch through holes are shown. This design allows the *Z Mount* to be positioned in vertical space by sliding up and down the threaded rods mounted into the *Base*. The mount is held in position by a total of six ¼" – 20 hex nuts which are screwed onto the threaded rods. Three nuts support the mount from below

while three nuts screw in and clamp the mount in place from above. Screwing the sets of nuts in a clockwise or counter-clockwise fashion enables mount adjustment in the vertical plane with high resolution.

Two identical bracket-like features extend from the top of the mount. These brackets provide a channel through which the *Z Sensor Rail*, with accommodating geometry, can slide to be adjusted forward and backwards. Fig. 14 shows one *Z Sensor Rail.*

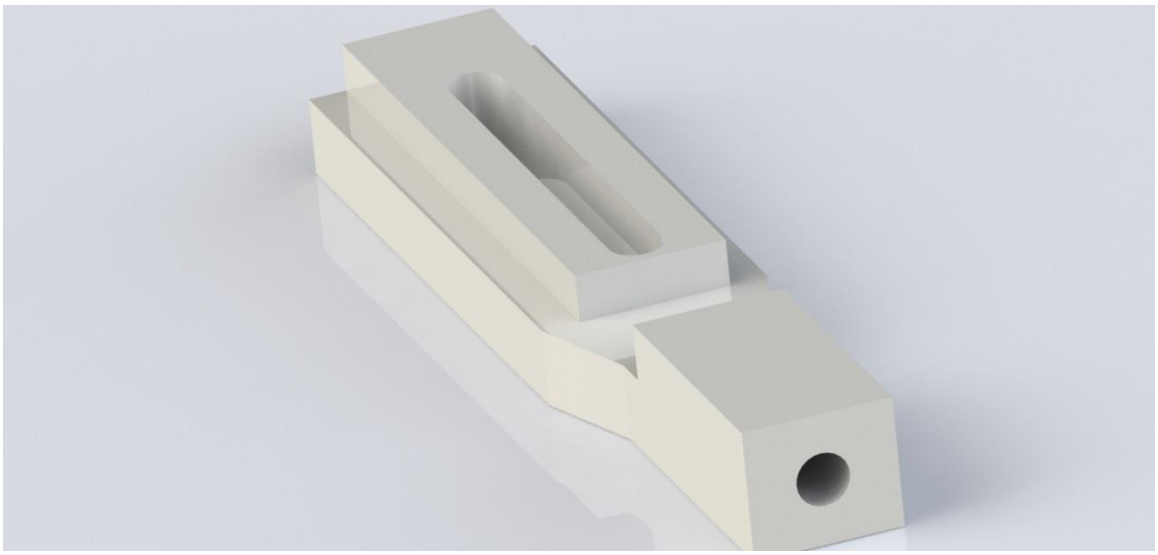

Fig. 14. Rendering of *Z Sensor Rail*

The slot seen in the sensor rail is a through-cut, allowing the sensor rail to be fixed in place by a socket head cap screw and mating hex nut. There are two holes seen drilled from the bottom of the *Z Mount* centered underneath each of the two sets of bracket/track features for the sensor rail. These holes are drilled to the outer diameter of the socket head cap screws and are not threaded. On the bottom end of the mount, the

holes are designed with a counter bore so that when the cap screw is mounted in place, the screw head top surface is flush with the bottom surface of the *Z Mount*.

The font face of the sensor rail is designed with a hole drilled and tapped to accept a socket head cap screw. In this fashion, a reflective object sensor is mounted to the sensor rail front face with a screw passing through the slot of the sensor and threaded into the hole to secure the sensor in place. The sensing face of the sensor is oriented downwards and senses the reflective white paper top surface of the *Probe* below. The final *Z Mount* with added *Z Sensor Rails* is shown in Fig. 15 without the sensors.

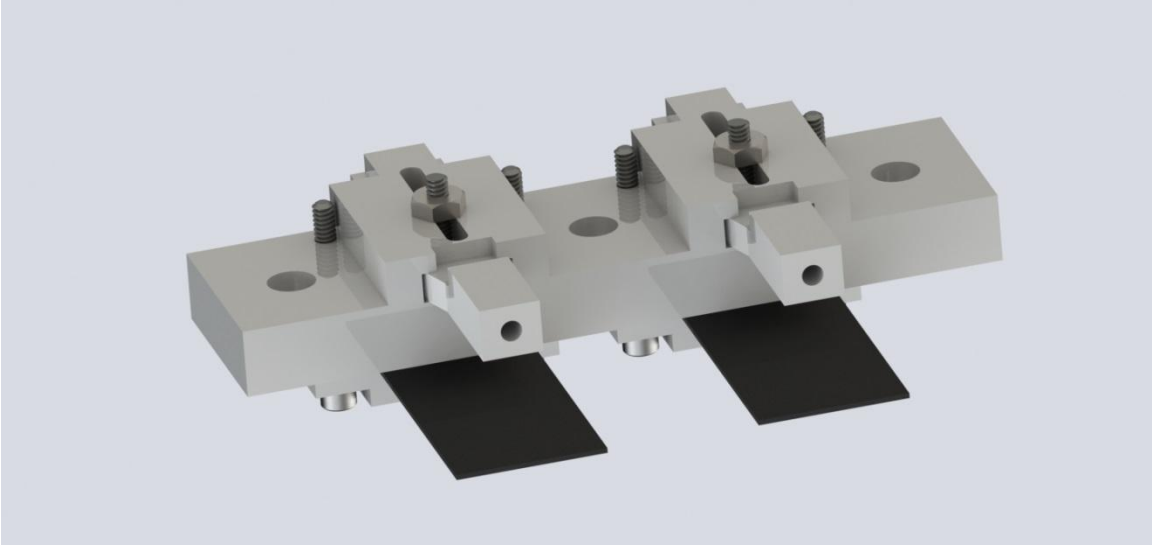

Fig. 15. *Z Mount* and *Z Sensor Rail* subassembly.

***Manufacture***

The *Z Mount* and *Z Sensor Rail* designs are concept designs for addition to the manufactured plant for this project. Machining would follow both manual and automated methods. The overall body of the *Z Mount* and *Z Sensor Rails* are machined using Rapid Prototyping. The slot features of the sensor rails can also be Rapid Prototyped.

## 2.3 Electrical Design & Development

### 2.3.1 Overview of Objectives

The overall objective was to design a circuit which conditions / prepares every sensor output signal for reception by the Data Acquisition System. The signal conditioning objectives were to perform level-shifting, noise filtering, and amplifying services to the sensor signal prior to DAQ retrieval. These objectives were met by the design of an analogue conditioning circuit external to the DAQ system.

### 2.3.2 Sensing System Design

Before design of the signal conditioning circuitry could take place, it was necessary to know more about exactly what signal the circuitry would be receiving. This dictated that the sensing system be fully developed.

Many sensor types were considered to quantify the motion output of the *Stage* and *Probe*s. The optimal choice was a reflective object sensor which operates with infrared optics. The feasibility of using commercially available, low-cost IR reflective object sensors for micro to sub micro scale position measurement and control has been investigated. Experimental results show that the performance of the IR sensors compares well with a commercial inductive sensor that costs significantly more [10]. Since cost and shelf life/ easily replaceable parts were restricting factors for this project, nano-scale precision expectations were slightly relaxed in favor of the reflective object sensor type.

The final sensor choice was Reflective Object Sensor model OPB704 manufactured by TT Electronics. Detailed information of this sensor can be found in *Appendix B. Reflective Object Sensor*.

In order to determine the exact sensor relationship between output voltage and sensing distance, each sensor underwent a data collection process. The experiment was run using an SPI digital caliper. The sensor was adhered to the static jaw using double sided adhesive tape. A straight edge was used to line up the sensor flat sensing edge in plane with the flat contact edge of the jaw. A thin piece of aluminum with the adhered white printer paper was used as the reflecting surface. This was adhered to the flat contact face of the moveable jaw using adhesive. Then the jaws were moved together, with the reflecting surface between them, and the caliper was calibrated to zero displacement. The setup was checked to ensure no gap between the sensor and reflecting surface.

The sensor was wired as shown in the final signal conditioning circuit of the next section, where the power input $V^+$ was 5 Volts. The experiment consisted of moving the reflective surface / jaw away from the static jaw with sensor by increments of 100 micrometers and measuring the sensor signal voltage output at each increment using an oscilloscope. The experiment was run for a distance range of 0 to 3.5 millimeters. The results are shown plotted in Fig. 16 for two separate sensors, designated *Sensor 1* and *Sensor 2*.

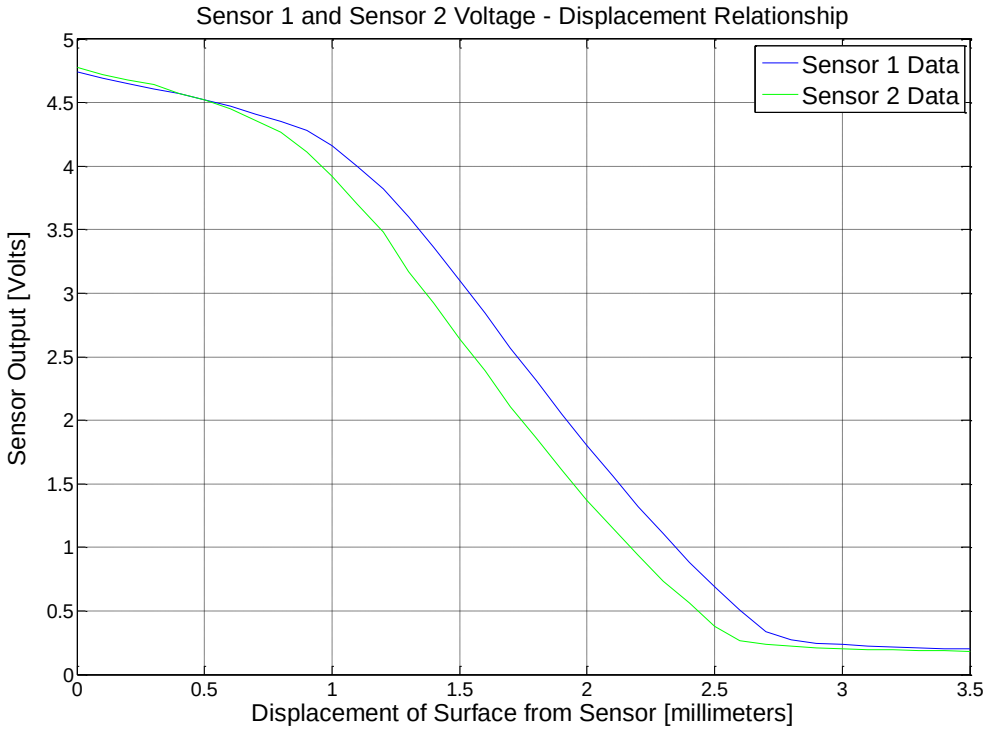


Fig. 16. Voltage-displacement relationship for *Sensor 1* and *Sensor 2.*

As is shown, the sensor outputs nearly the supply voltage of 5 volts when the reflecting surface is at a zero displacement from the sensor. The relationship can be described here as piecewise near-linearity. The optimal sensor-to-reflective surface displacement range in which to operate the sensor would be the large central linear portion of the curve with an approximate displacement range of 1.0 to 2.5 millimeters. This is the optimal range since the sensor exhibits the highest sensitivity here. Sensitivity refers to the magnitude by which the sensor output changes in response to an incremental change in surface to sensor distance. In another term, the sensor has the highest resolution in this range.

During control algorithm testing, prior to each control experiment start, the sensor is manually adjusted to provide an output voltage as close to the center of this displacement range as possible. Since the entire linear range is ~1.5 millimeters, this allows for tracking motion at amplitude of ~750 micrometers. This allowable sensing range is acceptable considering the theoretical maximum amplitude the bimorph can achieve for the *X* or *Y Direction* is sub 500 micrometers.

### 2.3.3 Conditioning Circuit Design

The first design question answered pertained to the type of electrical component(s) which would achieve the signal conditioning objectives of the circuit. Operational Amplifiers were employed as an obvious choice. An Op Amp can perform a great number of operations and can provide a wide variety of services to an electrical circuit *Base*d on its configuration. Op Amps are also readily available in integrated circuit form, making them a compact option.

The Operation Amplifier IC OP400 manufactured by Analog Devices was chosen. Further details about this Op Amp can be found in *Appendix C. Operational Amplifier*.

Fig. 17 shows the final signal conditioning circuit design to achieve the required objectives.

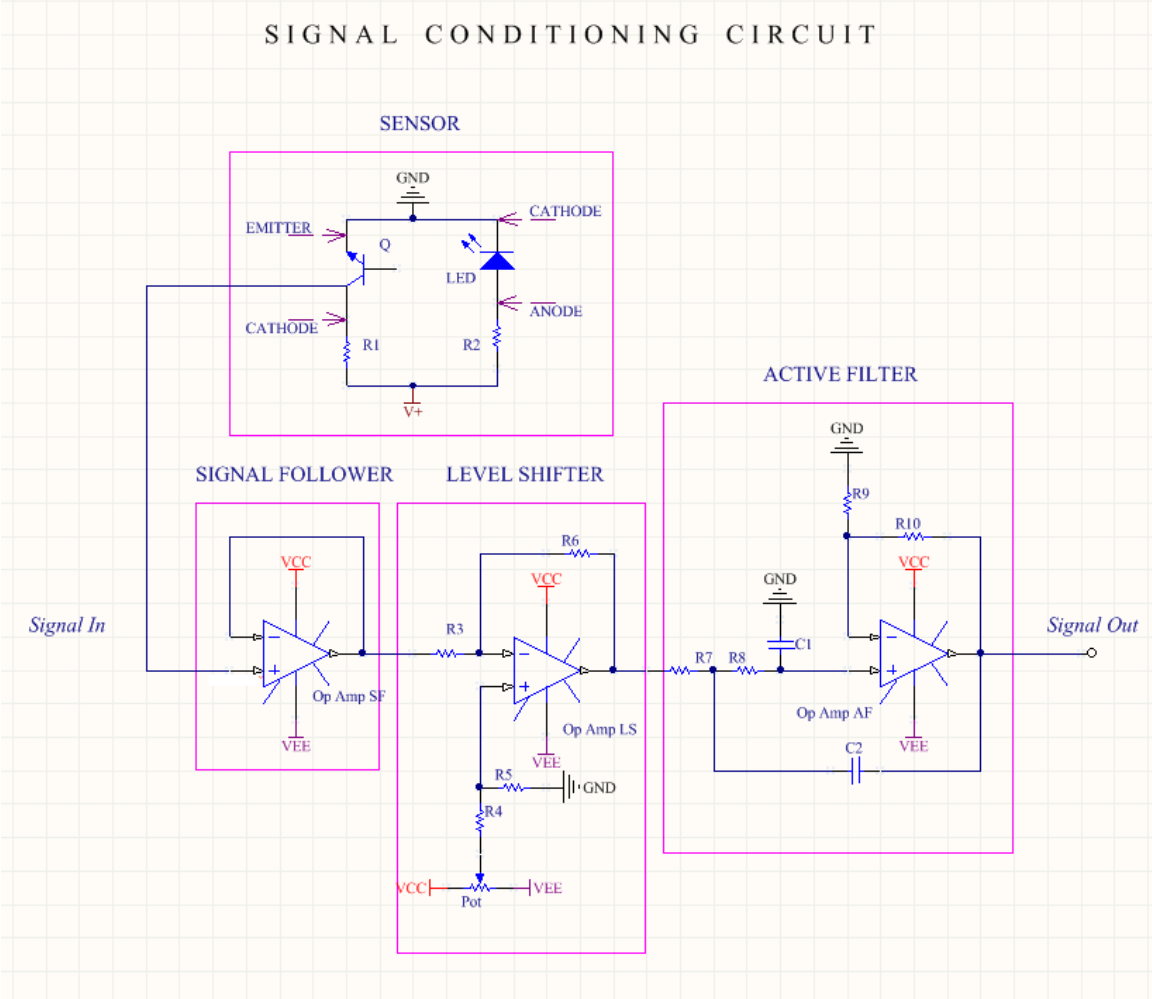


Fig. 17. Electrical schematic created with the software Altium Designer, Release 13.2.

Table 3 shows the list of all non-Op Amp circuit components used in the final design with corresponding values. The components are listed in alpha-numerical order.

| Component | Type | Sub Type | Value | |
|---|---|---|---|---|
| C1 | Capacitor | Ceramic | 0.1 | μF |
| C2 | | Ceramic | 0.1 | μF |
| Pot | Resistor | Variable | N/A* | |
| R1 | | Fixed | 15 | kΩ |
| R2 | | Fixed | 180 | Ω |
| R3 | | Fixed | 5.6 | kΩ |
| R4 | | Fixed | 220 | kΩ |
| R5 | | Fixed | 100 | kΩ |
| R6 | | Fixed | 5.6 | kΩ |
| R7 | | Fixed | 470 | kΩ |
| R8 | | Fixed | 2.2 | kΩ |
| R9 | | Fixed | 2.2 | kΩ |
| R10 | | Fixed | 2.7 | kΩ |
| $V^+$ | Power Source | DC | 5 | V |
| VCC | | DC - Symmetric | + 15 | V |
| VEE | | DC - Symmetric | - 15 | V |

*This value is frequently adjusted during level offset

Table 3. List of electrical circuit components.

The final circuit schematic is organized into four blocks. A reflective object sensor outputs the raw data signal derived from sensing either *Stage* or *Probe* motion, depending on the sensor designation. This raw signal comprises the Signal In line. Level shifting of the signal (removal of the DC offset) is accomplished by the Level Shifter block. Both noise removal and signal amplification are accomplished by the Active Filter block. The Signal Follower, in general, allows its input to be isolated from effects which happen on the downstream, or output, side of the block. A general discussion of the Signal Follower, Level shifter, and Active filter blocks is presented here. A detailed

analysis the design of two block sub-circuits, the Level Shifter and The Active Filter blocks, is provided in the *Appendix D. Level Shifter Design* and *Appendix E. Active Filter and Amplifier Design*, respectively.

In total, three Op Amps' were employed per sensor per signal. These are referred to as Op Amp SF (Signal Follower), Op Amp LS (Level Shifter), and Op Amp AF (Active Filter).

***Signal Follower Overview***

The original signal conditioning circuitry consisted solely of two operational amplifiers per raw sensor signal. The need for a signal follower configuration arose when it was desired to measure the raw unaffected sensor output signal to compare to the conditioned signal. The level shifter configuration actually affected both the output and input side to the Op Amp LS. The signal/voltage follower configuration was then added.

The name of this op amp-based sub-circuit derives from the ability of the output voltage, or signal, to follow exactly that of the input voltage/signal. This configuration creates a theoretical infinite input resistance, thereby permitting near perfect isolation between source and load and eliminates loading effects. This meant that the raw sensor signal, as an input to the Op Amp SF would be isolated from effects of the level shifter. The Op Amp SF was powered by a symmetric power source as indicated in the above circuit component table.

***Level Shifter Overview***

The second OP Amp was configured as a level shifter. The level shifter configuration of an Op Amp has the ability to add or subtract a DC offset to or from the signal. Level shifting of the DC component of the sensor output is necessary due to certain physical limitations of operational amplifiers.

In general, Op Amps are powered by DC voltage supplies which are usually symmetric. These are $VEE$ at -15 Volts and *VCC* at +15 Volts, as indicated in the previous table. The effect of limiting supply voltages is that amplifiers are capable of amplifying signals only within the range of their supply voltage. Furthermore, for most manufactured op amps, the limit is actually approximately 1.5 V less than the supply voltages. This has been verified in the project circuit. Any attempt to amplify a signal so that any region of the signal fall outside the supply voltage range will result in signal saturation and a "plateauing effect" of that signal region.

In order to maximize the amount to which the sensor signal can be amplified, the DC component, or constant voltage component, must be forced to zero. This was achieved through design of the Level Shifting sub-circuit.

***Active Filter & Amplifier Overview***

The third Op Amp was configured as a Low-Pass Sallen Filter. Several filters were proposed and analyzed before deciding on a final choice. Active filter configurations for op-amps were chosen due to their ability to shape the frequency response of the op-amp. This allowed the configuration not only to filter signal noise but amplify the signal as

well. This is opposed to the limitation in passive filters which can only condition signal noise.

The filter choice was further honed by order selection. The order of a filter is equal to the order of the differential equation that describes the input-output relationship of the filter. In general, the higher the order, the faster the transition from pass band to stop band, but at the cost of greater phase shifts and amplitude distortion. The second order Low-pass Sallen filter was the chosen design for this project.

The control of the frequency response is characteristic of three parameters, Quality Factor $Q$, cutoff frequency $\omega_C$, and gain $K$. A very desirable property of the Sallen filter is the fact that the low-frequency gain of the filter is independent to the cutoff frequency. The gain was designed to amplify the signal within the limiting bounds of +/- 10 Volts, which was the DAQ board limiting input voltage. The cutoff frequency was chosen to be twenty times an absolute maximum operating frequency of 30 Hz, setting the goal value at 600 Hz. The last parameter, Quality Factor, was designed by analyzing the frequency response, using the designed cutoff frequency and gain, for several different Quality Factor values. The choice of $R_1, R_2, C_1,$ and $C_2$ followed from an iterative process such that component values matched well with existing manufactured values available.

# 3. Implementation & Evaluation of Advanced Iterative Learning Control Techniques

## 3.1 Overview of Objectives

As was previously outlined, the overall objectives were to achieve nano-scale precision of motion control for a system of large size and high speed. Chapter 2 described the design and manufacture of the plant system and outlined speed and amplitude motion characteristics for the mass being vibrated. This current chapter describes how this was achieved.

## 3.2 Control Law Approach

To achieve motion control of the *Stage* and *Probe* in this project, two inversion-based iterative learning control (IIC) techniques were employed. The first is the recently developed Model-Free Inverse-Based Iterative Learning Control method (MIIC). The second approach is the novel High-Order Difference Model-Free Iterative Learning Control (HODMIIC). Iterative learning control (ILC) methods have eben shown to be efficient in repetitive output tracking [11-15]. This includes the ability of ILC methods for rapid convergence of the iterative control input by quantifying and accounting for the effect of dynamics uncertainty [16]. However, both MIIC and HODMIIC are model-free control methods, signifying the elimination of the dynamics modeling process [16].

Eq. 14 represents the MIIC law.

$$u_k(j\omega) = \begin{cases} \alpha y_d(j\omega), & k = 0 \\ \dfrac{u_{k-1}(j\omega)}{y_{k-1}(j\omega)} y_d(j\omega), & k \geq 1, \end{cases} \tag{13}$$

Here, $u$ and $y$ represent the system input and output respectively. The subscripts $d$ and $k$ refer to "desired", in terms of the desired output, and the current iteration of tracking control. The $\alpha$ term is a prechosen constant which applies to the first, or zeroth, iteration only, and is restricted not to be made zero. Typically, this value is chosen as the inverse gain of the system, as described in Sec. 3.3.1 *Control Law Implementation*.

In general the input and output are functions of $j\omega$, denoting they are Fourier transforms of the input and output signals. Thus, the IIC law is implemented as a frequency-domain formulation scheme. The inverse dynamics model portion, or $u_{k-1}/y_{k-1}$, is updated by using the quantified input-output data from the sensors and data acquisition system during each iteration. In the frequency domain formulation, this is done only at the frequencies where tracking is sought. Through this formulation, model error is essentially removed and the noise effect on the system can be ignored.

The HODMIIC control law is show in Equations 15 and 16.

For $k \leq 1$:

$$u_k(j\omega) = \begin{cases} \alpha y_d(j\omega), & k = 0 \\ \dfrac{u_{k-1}(j\omega)}{y_{k-1}(j\omega)} y_d(j\omega), & k = 1 \end{cases} \tag{14}$$

For $k > 1$:

$$u_k(j\omega) = u_{k-1}(j\omega) + \frac{\rho}{\sum\beta_i}\left(\beta_1 \frac{u_{k-1}(j\omega) - u_{k-2}(j\omega)}{y_{k-1} - y_{k-2}} + \beta_2 \frac{u_{k-2}(j\omega) - u_{k-3}(j\omega)}{y_{k-2}(j\omega) - y_{k-3}(j\omega)} + \cdots + \beta_{k-1} \frac{u_1(j\omega) - u_0(j\omega)}{y_1(j\omega) - y_0(j\omega)}\right)(y_d(j\omega) - y_{k-1}(j\omega)) \quad (15)$$

The new terms presented here are the "Forgetting Coefficient", $\beta_i$, and $\rho$. The Forgetting Coefficient follows the pattern of Eq. 17.

$$\beta_i = \beta^i \;\; \forall \;\; 0 < i \leq k-1 \quad (16)$$

Here, $\beta$ is baseline forgetting coefficient defined at the start of the control algorithm, and $i$ ranges from 1 to the integer value of the current iteration, $k$. Following this rule, the iterative control law pattern is as follows.

$$u_0 = \alpha y_d$$

$$u_1 = \frac{u_0}{y_0} y_d$$

$$u_2 = u_1 + \frac{\rho}{\beta_1}\left(\beta_1 \frac{u_1 - u_0}{y_1 - y_0}\right)(y_d - y_1)$$

$$u_3 = u_2 + \frac{\rho}{(\beta_1 + \beta_2)}\left(\beta_1 \frac{u_2 - u_1}{y_2 - y_1} + \beta_2 \frac{u_1 - u_0}{y_1 - y_0}\right)(y_d - y_2)$$

$$u_4 = u_3 + \frac{\rho}{(\beta_1 + \beta_2 + \beta_3)}\left(\beta_1 \frac{u_3 - u_2}{y_3 - y_2} + \beta_2 \frac{u_2 - u_1}{y_2 - y_1} + \beta_3 \frac{u_1 - u_0}{y_1 - y_0}\right)(y_d - y_3)$$

$$\vdots$$

The first dashed outline shows the portion of the control law which lies in the purely MIIC regime, and the second dashed outline shows the portion of the control law which follows the main HODMIIC algorithm. For simplicity, the $'j\omega'$ notation has been dropped but is implied.

For each iteration of the HODMIIC regime, the new input generated for the plant begins at a baseline value, that is, the previous iteration input signal. Added to this signal is a correcting factor, which makes the newly generated input an improvement over the previous iteration input by generating an output which accumulates less error than the previous iteration. The correction factor is based on a weighted average of difference-based successive inverted dynamics terms. A key difference between MIIC and HODMIIC is in the amount of tracking history evaluated. In MIIC, only the previous iteration results are used to generate the current iteration signal. In contrast, HODMIIC uses the complete history of iterated results, since the first iteration, and averages them. This speaks to the HODMIIC regime being of "High-Order". The Forgetting coefficient takes care of weighting the average. Typical baseline values for the Forgetting Coefficient range from 0.1 to 0.3, and therefore the power law dictating the $\beta_i$ values result in successively smaller values for an increase in $i$. It is therefore seen that inverse transfer function terms representing the results of less-recent successive iterations are multiplied with $\beta_i$ values of smaller magnitude. Thus, these terms influence the current signal generation less than the more recent history of terms. To complete the weighted average, the added inverse transfer function terms are divided by the summation of all generated $\beta_i$ values, $\sum_{i=1}^{k-1}\beta_i$, to normalize the correcting factor. A difference term

between the desired and last iterative output is multiplied. This is required since the weighted average occurred with inverse transfer function terms. What is left is in essence a corrective input or $'u'$ factor to be added to the last iteration input to generate an improved input.

The last term to consider is $\rho$, which alters this corrective factor. It is seen that reducing $\rho$ reduces the convergence speed but results in more accurate tracking, and vice versa. This is evident in the control law, as reducing $\rho$ makes smaller the corrective term, thus reducing the change/difference in input signal between two successive iterations, providing a slow convergence. A Typical baseline/start value for $\rho$ is 0.5. During experimentation, the value has been tuned to provide a balance between tracking accuracy and speed of tracking convergence. In general, the $\rho$ term, just like the Forgetting Factor, make pliable the nature of the HODMIIC algorithm. These terms allow the end user to tune the behavior of the control algorithm in favor of the user's convergence speed and accuracy-based needs.

In this project, a focus was put on applying each of the two ILC schemes for controlling the plant via bimorphs. This allowed a compare and contrast of the two schemes. As is shown through experimental results in the following section, HODMIIC proves superior over the MIIC algorithm. The reason HODMIIC outperforms MIIC lies with how the algorithm specifically handles repeated and random errors. Through the addition or averaging portion of the control law, the random portion of error is removed while the repeated errors are integrated. HODMIIC uses this integration of repeated errors to continually correct the next generation input and thereby improves on MIIC by having visibility over the entire tracking history.

## 3.3 Implementation & Evaluation

### 3.3.1 Control Law Implementation

The block diagram for implementation of the MIIC or HODMIIC control laws is shown in Fig. 18.

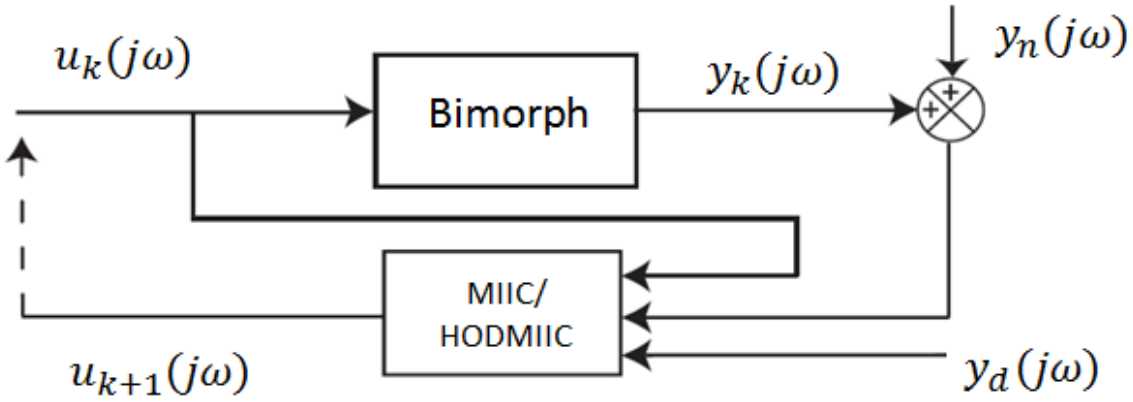


Fig. 18. Block diagram representing control law implementation.

The dashed arrow type feeding the control-updated input into the system signifies the offline mode in which these control algorithms operate. That is, each iteration is comprised of the system in dynamic and static regime. The control law updates and applies the system input to a static system.

As was discussed extensively in Sec. 2.2.1 *Developing a General Plant Model*, the *X* and *Y Directions* are coupled to each other. Figures 19 and 20 below show the *X*

*Direction* dynamics with the Y to X coupling dynamics effect as well as *Y Direction* dynamics with the X to Y coupling dynamics effect.

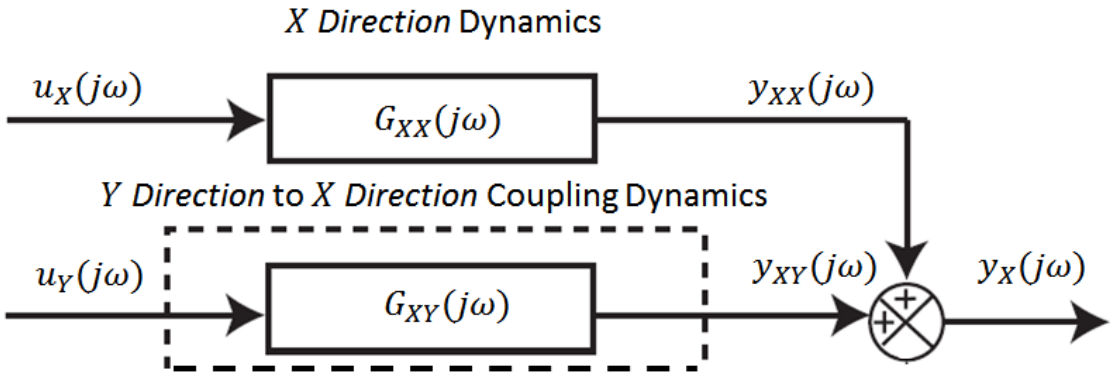


Fig. 19. *X Direction* dynamics with the Y to X coupling dynamics effect.

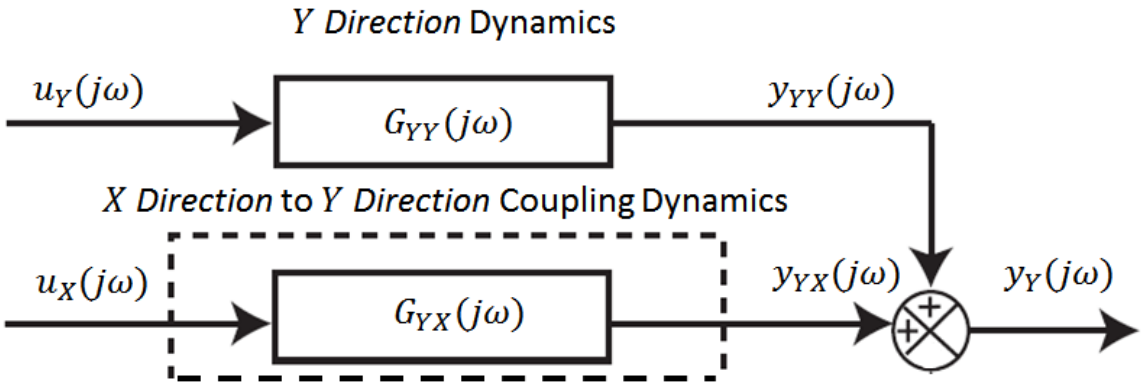


Fig. 20. *Y Direction* dynamics with the X to Y coupling dynamics effect.

Two main positioning regimes were experimented on to evaluate the effectiveness of MIIC and HODMIIC as control laws able to achieve high precision tracking over a

range of plant motion. These two regimes were Single-Axis positioning and Dual-Axis simultaneous positioning. Specifically, since the *Z Direction* model components were presented as a concept design and not actually manufactured, the *Stage* and *X and Y Bimorphs* were the pertinent system plant during experimentation. The control flow architectures for both the Single-Axis and Dual-Axis positioning regimes are represented in Figures 21 and 22.

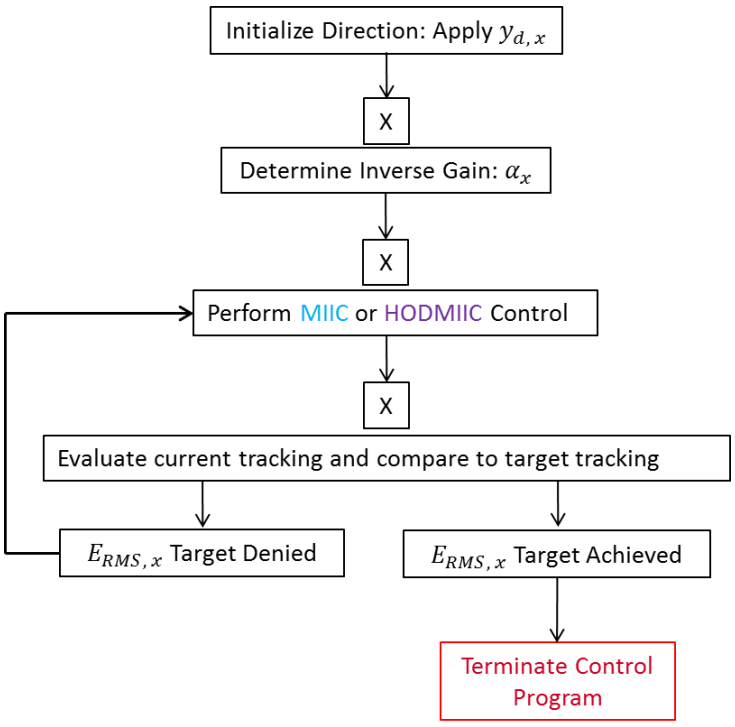


Fig. 21. Single-Axis control flow architecture. Example in *X Direction.*

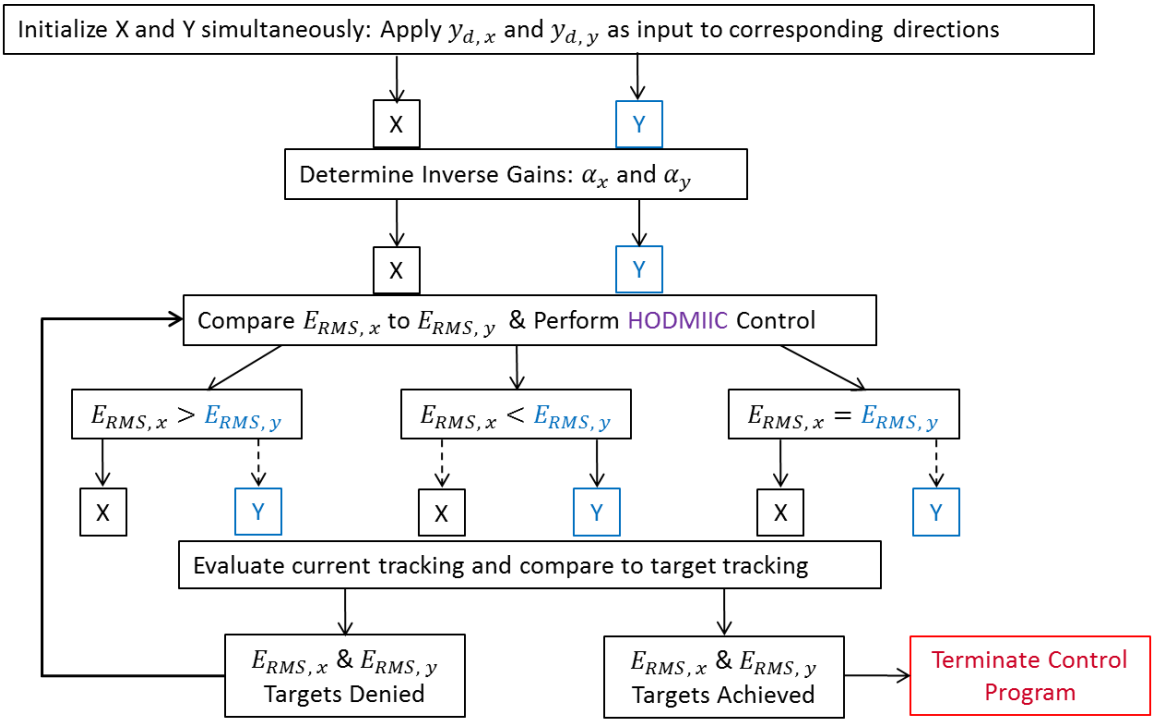


Fig. 22. Dual-Axis control flow architecture representing the Coupling-Quantification-Free Oscillatory Control Approach with the HODMIIC algorithm.

For both single-axis and dual-axis positioning, the very first task involves initializing the active direction(s) by inputing soley the corresponding desired signal. The output is used to calculate the inverse-gain alpha value(s). The zeroth iteration follows with an input defined as alpha multiplied by the desired signal for both MIIC and HODMIIC.

The architecture between the single-axis and dual-axis positioning flows differentiates after the zeroth iteration. For single-axis control, only one direction is active throughout the control attempt. Either MIIC or HODMIIC is used in an iterative

process until the desired error tareget for the active direction is achieved. At this point the user can terminate the control attempt.

For Dual axis motion, a novel concept was developed to compensate for the inherent coupling effect of the *X* and *Y Directions.* The approach is called the Coupling-Quantification-Free Oscillatory Control Approach. This approach actively updates only one direction at time. Quantification-free here dictates that the coupling signal is neither quantified nor pertinent for adequate simultaneous motion control. Figure 22 outlines this approach and shows HODMIIC as the sole control algorithm. This is due to the superiority of the HODMIIC regime, as is discussed in Section 3.3.3 *Tracking Results & Discussion.*

The zeroth iteration is the only iteration in which both directions are simultaneously updated, or active. In each subsequent iteration, the control algorithm updates only the input to that direction whose previous iterative input resulted in greater tracking error. It is by arbitrary convention that the *X Bimorph* / *X Direction* receive an updated control input should the tracking error be equivalent between the *X* and *Y Directions* for any given iteration. The direction which receives an updated control input is considered to be control-active for that iteration. The control-inactive direction receives the same input as it received in the previous iteration. The oscillatory nature of this method is inherent in the prognosis that a control-active direction be driven to a lower error than the control inactive direction, resulting in a switch of which direction is control active, a cycle which would endure for the life of the experiment.

This control law implementation for dual axis control is not only novel, but efficient in tracking each direction simultaneously under planar motion since there is no need to quantify system coupling. This raises the overall efficiency of a control system where time is already saved due to both MIIC and HODMIIC control laws taking a model-free approach.

### 3.3.2 Plant Dynamics

Two frequency response analyses were completed regarding *Stage* motion in the *X Direction* and *Y Direction.* The frequency responses evaluated are shown in Table 4.

| Frequency Response | Active | Inactive | Measured |
|---|---|---|---|
| *X Direction* | *X* | *Y* | *X* |
| *X* to *Y* Coupling | *X* | *Y* | *Y* |

Table 4. State of bimorphs for both evaluated frequency responses.

The active direction is defined as that direction whose designated bimorph receives an input signal. The inactive direction is defined as that direction whose designated bimorph receives no input signal. The measured column designates which direction is measured and plotted for that particular frequency response.

To generate the data to evaluate each frequency response, varying band-limited white noise signals were generated and subsequently input to the active direction. For each frequency response test, the input was sent and data collected over a loop of four

different white noise signals. Each white noise signal was generated over a frequency range of 5 to 700 Hertz and had a time-domain duration of 5 seconds. The white noise signals varied in their amplitude parameter. The amplitude parameters used were 1 , 1.16, 1.3, and 1.5 Volts for the respective four signals. However, as can be seen in the provided code of the appendix, the actual maximum amplitude was decreased in in creation of the white noise signal. Since the amplifier gain is 50, a voltage magnitude input greater than 1 volt would violate the maximum allowed voltage magnitude of 50 Volts to the bimorphs wired in parallel configuration. Several program checks ensured that the bimorph operation thresholds were not violated. Fig. 23 shows the set of white noise signals used for each frequency response test.

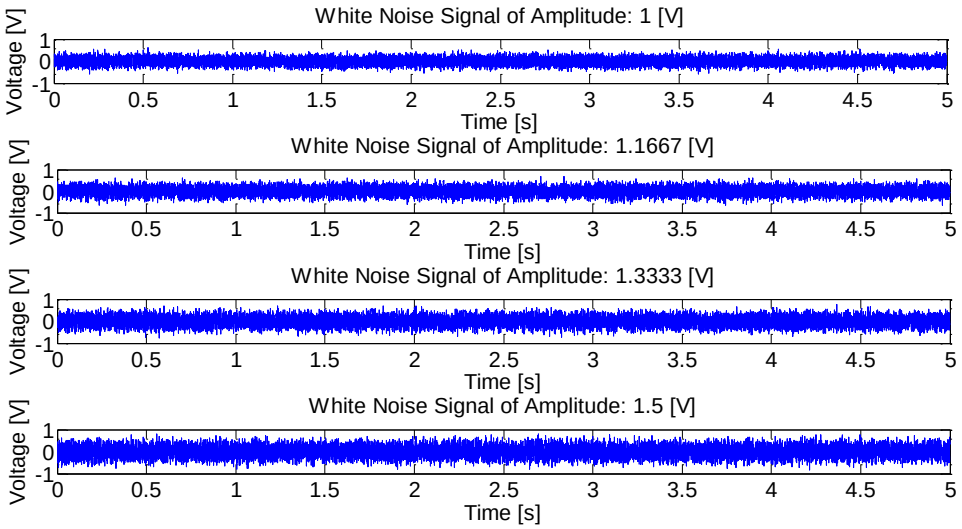


Fig. 23. The set of four white noise signals used for each frequency response test.

The resulting frequency response figures are now represented. Both frequency response tests are represented in a total of two plots. The first plot represents the raw

data unconditioned by the built-in MATLAB smoothing functions. The second plot represents that data as plotted using build in *smooth( data , span )* which smooth's the data *data* in moving average fashion using *span* as the number of points used to compute each element of the function output. In this case, the data is conditioned with a span of 20.

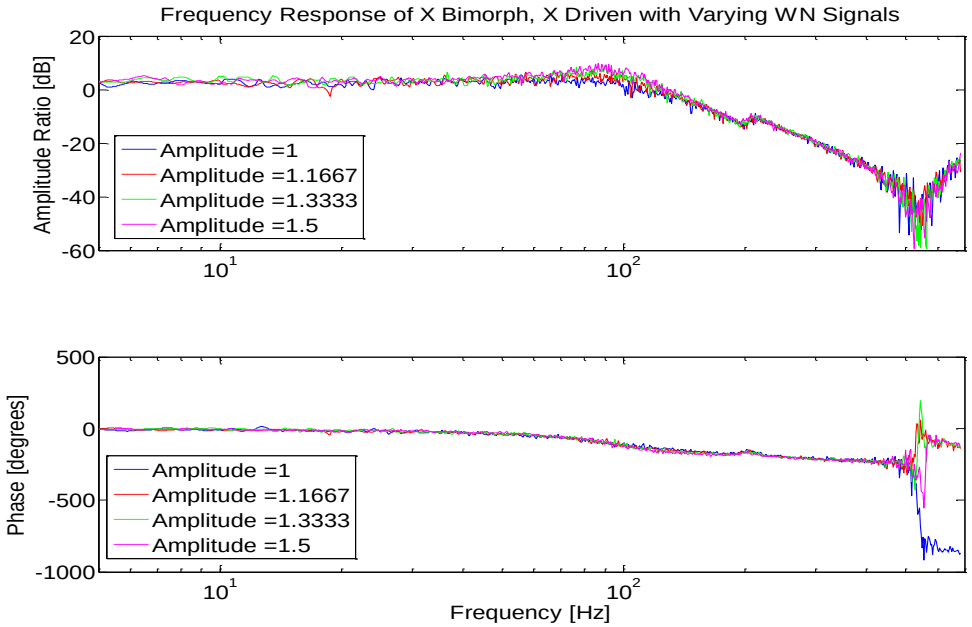


Fig. 24. Direct Frequency Response of *X Bimorph* plotted with raw data.

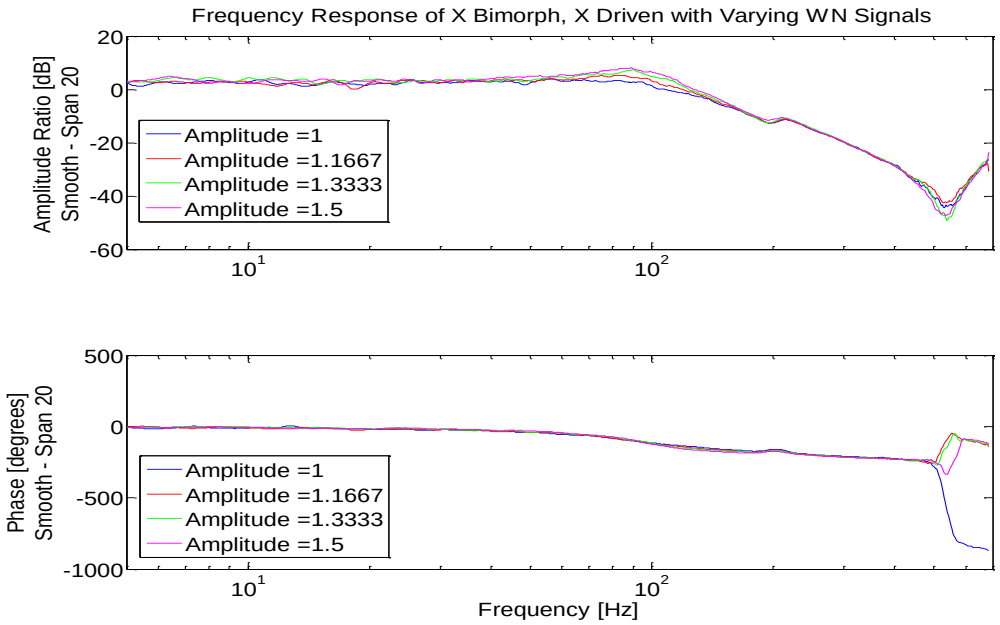


Fig. 25. Direct Frequency Response of *X Bimorph* plotted with smoothed data.

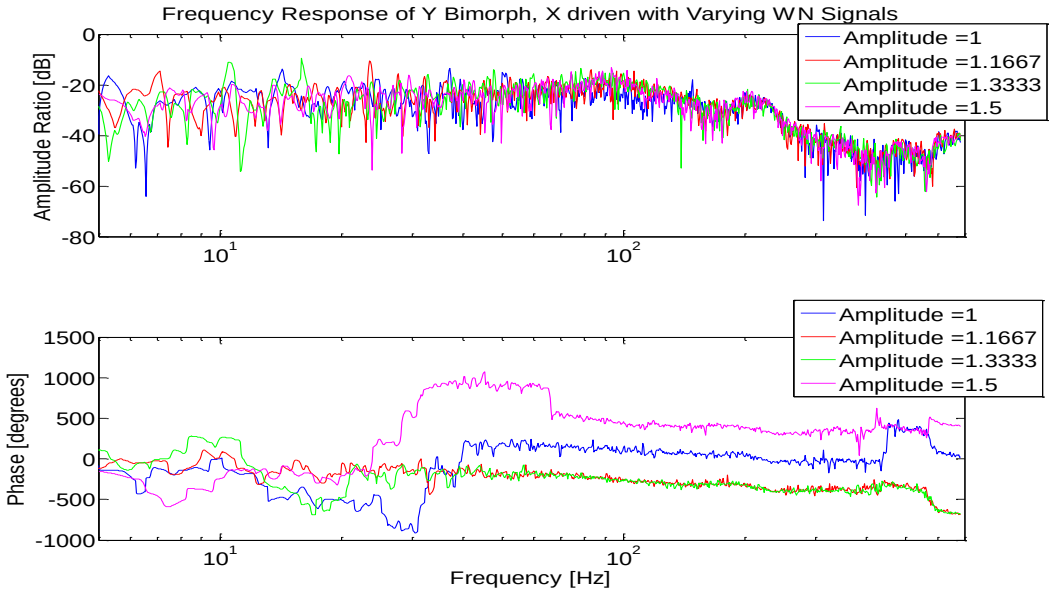


Fig. 26. Coupling Frequency Response of *Y Bimorph* plotted with raw data.

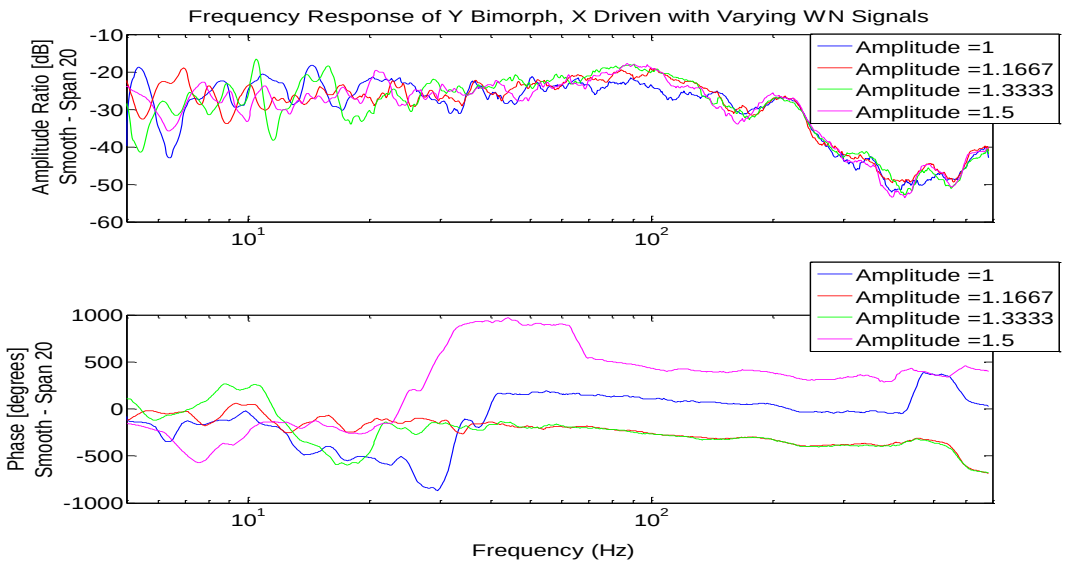


Fig. 27. Coupling Frequency Response of *Y Bimorph* plotted with smoothed data.

The tracking results are shown in general to represent *Stage* dynamics both for a driven direction and coupling dynamics from the response of the non-driven direction. The dynamics results provide a valuable insight for *Stage* behavior. For the driven direction, amplitude ratio magnitudes range from 1 to 3 throughout most of the lower frequencies leading up to the resonant region. In contrast, the amplitude ratio for the coupling response, that is non-driven output to driven input, ranges from 0.1 to 0.001. The non-driven output is significantly smaller than the driven input. These results verify the success of *Stage* design and bimorph interfacing design in greatly reducing coupling effects between the *X* and *Y Directions* of motion.

The resulting resonant peak also provides a caution for tracking results and control algorithm testing. In general, the resonant peak of the magnitude plot occurs around 80 – 100 Hertz. This represents the region of the fundamental resonant

frequency, or the lowest resonant frequency of the *Stage*-bimorph system. In addition, resonant effects can be present at harmonics of the fundamental frequency, represented by integer multiples of the frequency. These resonant effects are not of particular interest due to their basis at frequencies outside the operating regime of the system. However, a class of harmonics, called sub-harmonics, is of interest. Taking fractional multiples of the fundamental frequency, say a multiple of $1/4$, yields a sub-harmonic which falls in the range of 20 to 25 Hertz. In fact, the possibility exists that this particular sub-harmonic is not negligible, as is evident in Sec. 3.3.4 *Tracking Results & Discussion.*

### 3.3.3 Tracking Results & Discussion

In order to thoroughly test the ability of both the MIIC and HODMIIC control algorithms, each algorithm was employed to track both small and large-amplitude trajectories across a range of frequencies as implemented for the single-axis positioning regime. The superior HODMIIC algorithm was then targeted for control of the dual-axis positioning regime, where large-amplitude trajectories were tracked across a range of

***Single-Axis Positioning Results***

In order to gather an accurate representation across the objective operating range of *Stage* motion, triangle waves of two amplitudes, 30 and 250 micrometers, were defined, with each amplitude being tested at 5, 10, and 15 Hertz with an additional attempt at 25 Hertz. Thus a total of eight different triangle waves were tracked. The input signals were

applied with a total duration of 3.5 seconds which consisted of 1 second zero signals appended to each end of the 1.5 second triangle signal. Each of these waveforms were applied and tracked in two separate experiments, one for each applied control algorithm. The *X Direction* was arbitrarily chosen to be the example direction for single-axis control. For all experiments, the baseline forgetting factor, $\beta$, was set at 0.03 and the factor $\rho$ was set at 0.05.

The results for each experiment and each algorithm are compared on an error basis. For this project, RMS error based on voltage is calculated for every iteration using the built in MATLAB function *norm( )*. Eq. 18 represents the two-norm based RMS error calculation for a given iteration $k$.

$$E_{RMS,\ k} = \frac{\|y_d - y_k\|_2}{\sqrt{n}} \tag{17}$$

$E_{RMS,\ k}$ represents the RMS error for a given iteration $k$, $y_d$ and $y_k$ represent the desired output and current iteration output, and $n$ is the number of data points in the desired output vector.

The results for MIIC and HODMIIC are compared in two instances: one for the low-amplitude case of 30 $\mu$m and another for the large amplitude case of 250 $\mu m$. For each case, one table and two figures are presented for comparison. The table compares sets of $E_{rms}$ data for each control algorithm side by side for each of the frequencies of desired signals tracked. The first figure plots detailed regions of the experimental tracking results for each control algorithm across the frequencies. The tracking results

for the single lowest-error iteration are shown. The second figure compares the $E_{rms}$ for each algorithm across each frequency.

To begin with, the small-amplitude tracking case is evaluated for both the MIIC and HODMIIC control algorithms. The tracking results of the triangle trajectory for 5, 10, and 15 Hertz are shown in Figure 28, and compared through raw data in Table 5 and plotted form in Figure 29. The tracking results for a triangle trajectory of 25 Hertz were redundant and omitted for simplicity.

| Iter. No. | *$E_{rms}$ For 30 μm Amplitude Triangle Wave* | | | | | |
|---|---|---|---|---|---|---|
| | 5 Hz | | 10 Hz | | 15 Hz | |
| | *MIIC* | *HODMIIC* | *MIIC* | *HODMIIC* | *MIIC* | *HODMIIC* |
| 1 | 0.01492 | 0.01544 | 0.01132 | 0.01154 | 0.00976 | 0.01193 |
| 2 | 0.00996 | 0.01149 | 0.00999 | 0.01023 | 0.00925 | 0.01009 |
| 3 | 0.00931 | 0.00984 | 0.01034 | 0.00906 | 0.00791 | 0.01014 |
| 4 | 0.01418 | 0.00800 | 0.00958 | 0.00752 | 0.00916 | 0.00997 |
| 5 | 0.01038 | 0.00546 | 0.00943 | 0.00646 | 0.00798 | 0.00912 |
| *Minimum $E_{rms}$, **Iter. No.*** | | | | | | |
| | 0.00752, **19** | 0.00209, **36** | 0.00789, **19** | 0.00245, **45** | 0.007175, **21** | 0.00244, **40** |

Table 5. $E_{rms}$ for 30 $\mu$m amplitude triangle wave tracking's from 5 to 15 Hz. The error is compared between MIIC and HODMIIC during the first five iterations in the upper rows. The bottom row shows the lowest achieved error and the iteration during which it was achieved.

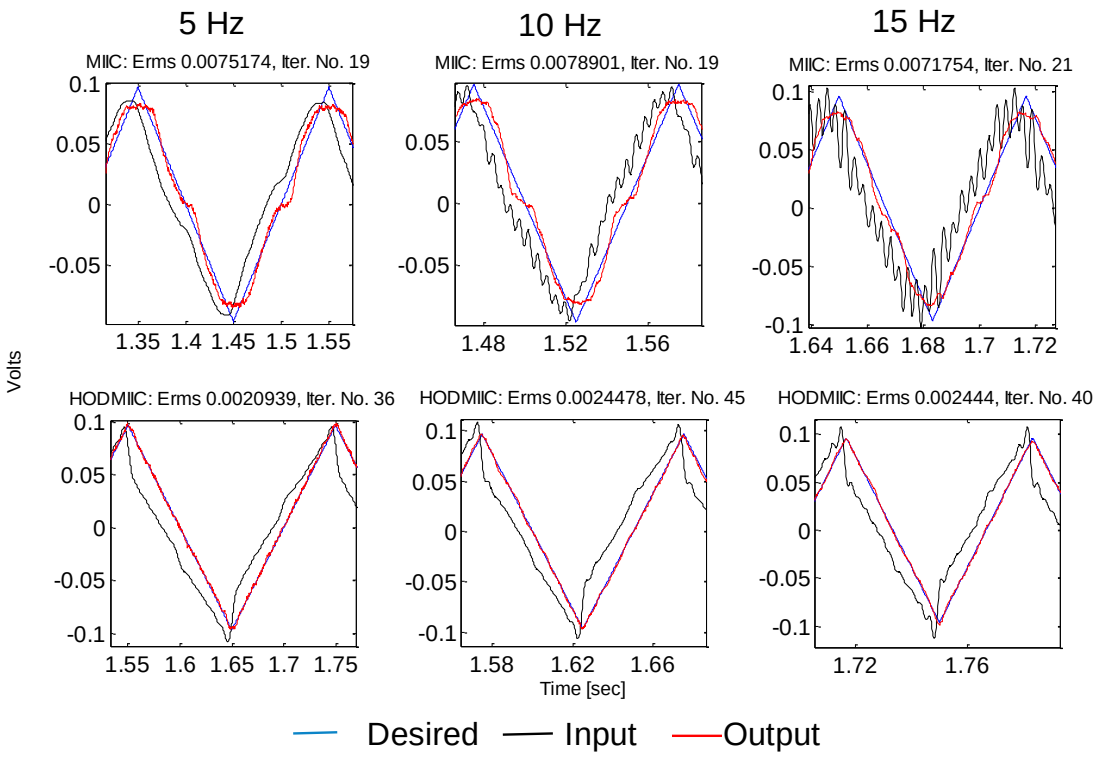


Fig. 28. Experimental results: Comparison of the output tracking obtained by using the MIIC control law (top row) and HODMIIC control law (bottom row) for a triangle wave of 30 $\mu$m amplitude and 5, 10, and 15 Hz. Plots represent single iteration results during which the minimum $E_{rms}$ was achieved.

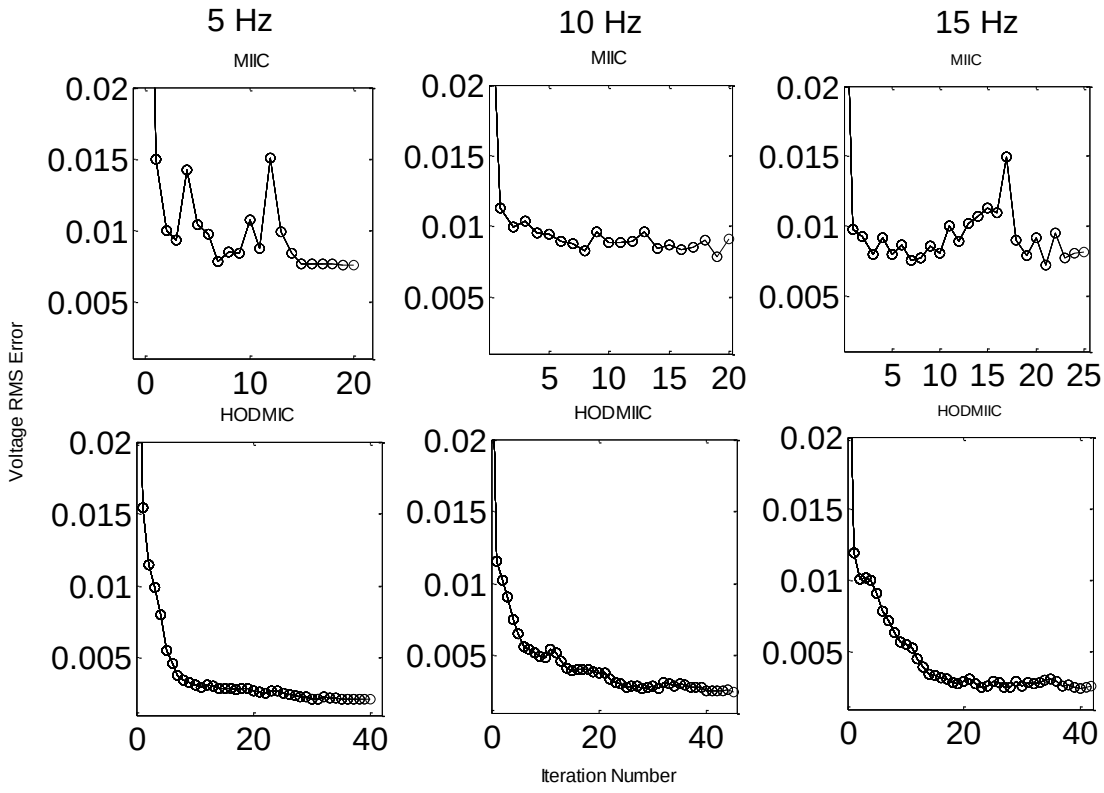


Fig. 29. Comparison of the $E_{rms}$ versus iteration number results as achieved by the MIIC control law (top row) and HODMIIC control law (bottom row) for tracking a 30 $\mu$m amplitude triangle wave from 5 to 15 Hz. Y-axis range is constant between all figures for ease of comparison.

The results verify that each control law is capable of achieving a normalized tracking error below the desired upper threshold of 0.05 within a desired operation range of *Stage* motion. In fact, for single axis control, both MIIC and HODMIIC consistently drove the error to around 0.01 and less after just five iterations. In this way, MIIC and HODMIIC are control laws capable of both high tracking precision and high convergence speed.

The advantages of a complete and weighted tracking history in influencing the iterative control input are clear in the comparison between MIIC and HODMIIC. Although the tracking convergence for MIIC is considered successful, the tracking convergence for HODMIIC is even more so. Considering a large portion of the overall plant motion, HODMIIC consistently results in a minimum tracking error of 0.0026 or lower. The exception comes in the high speed case where a signal of 25 hertz was tracked with HODMIIC achieving a minimum error of 0.00376. The results are omitted here; however they follow the basic trend for both algorithms. System dynamics become more demanding on the control algorithm for the high speed case as the bimorph is driven to navigate the sharp corners of the triangle peaks and troughs at high speed.

Both MIIC and HODMIIC show the ability to consistently track the sharp triangle peaks and troughs below the error threshold. In order to achieve the desired triangle trajectory, the input waveforms contain multiple frequency components. The effect is a subtle one at lower frequencies as the momentum of the bimorph tip at the peaks and troughs of the trajectory is much lower, making it much easier to track these quick changes in speed and direction. However, for desired signals of increasingly higher frequency, both MIIC and HODMIIC provide input signals with higher frequency wave components embedded in the overall triangular input. These higher frequency undulations also become higher in amplitude as the desired waveform frequency increases. It is necessary for the iterated inputs to be increasingly dominated by high frequency components in order for the control laws to consistently track the desired triangle corners.

It is also noted that HODMIIC iterated inputs show a slower and more stable rise in the incorporation of higher frequency undulations over most of the operation range, whereas the increase of these components in the MIIC outputs is more sudden and drastic. This speaks to HODMIIC showing more control over the demanding system dynamics for the *Stage* at a high speed.

The following results evaluate the large-amplitude tracking case for both the MIIC and HODMIIC control algorithms. The tracking results of the triangle trajectory for 5, 10, and 15 Hertz are shown in Figure 30, and compared through raw data in Table 6 and plotted form in Figure 31. Neither the MIIC nor the HODMIIC control laws were able to successfully track the large-amplitude triangle trajectory at 25 Hertz. This outcome is discussed below.

| Iter. No. | $E_{rms}$ For 250 μm Amplitude Triangle Wave | | | | | |
|---|---|---|---|---|---|---|
| | 5 Hz | | 10 Hz | | 15 Hz | |
| | *MIIC* | *HODMIIC* | *MIIC* | *HODMIIC* | *MIIC* | *HODMIIC* |
| 1 | 0.05452 | 0.05578 | 0.02053 | 0.02043 | 0.02778 | 0.02648 |
| 2 | 0.02351 | 0.03744 | 0.02890 | 0.01538 | 0.03771 | 0.01945 |
| 3 | 0.01655 | 0.02857 | 0.01970 | 0.01225 | 0.03219 | 0.01861 |
| 4 | 0.01523 | 0.02285 | 0.01555 | 0.00843 | 0.04020 | 0.01711 |
| 5 | 0.01375 | 0.01561 | 0.01432 | 0.00641 | 0.02533 | 0.02175 |
| *Minimum $E_{rms}$, **Iter. No.*** | | | | | | |
| | 0.01125, **19** | 0.00402, **20** | 0.00953, **13** | 0.00373, **17** | 0.01772, **13** | 0.00684, **24** |

Table 6. $E_{rms}$ for 250 $\mu$m amplitude triangle wave tracking's from 5 to 15 Hz. The error is compared between MIIC and HODMIIC during the first five iterations in the upper rows. The bottom row shows the lowest achieved error and the iteration during which it was achieved.

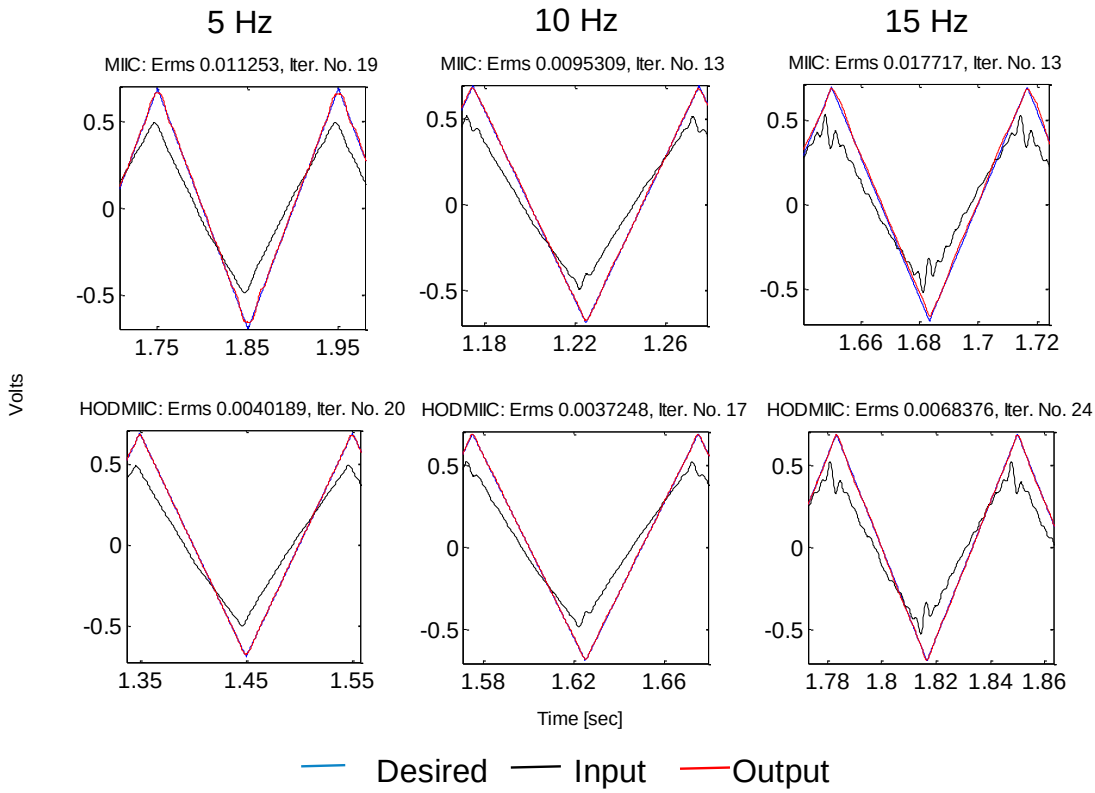


Fig. 30. Experimental results: Comparison of the output tracking obtained by using the MIIC control law (top row) and HODMIIC control law (bottom row) for a triangle wave of 250 $\mu$m amplitude and 5, 10, and 15 Hz. Plots represent single iteration results during which the minimum $E_{rms}$ was achieved.

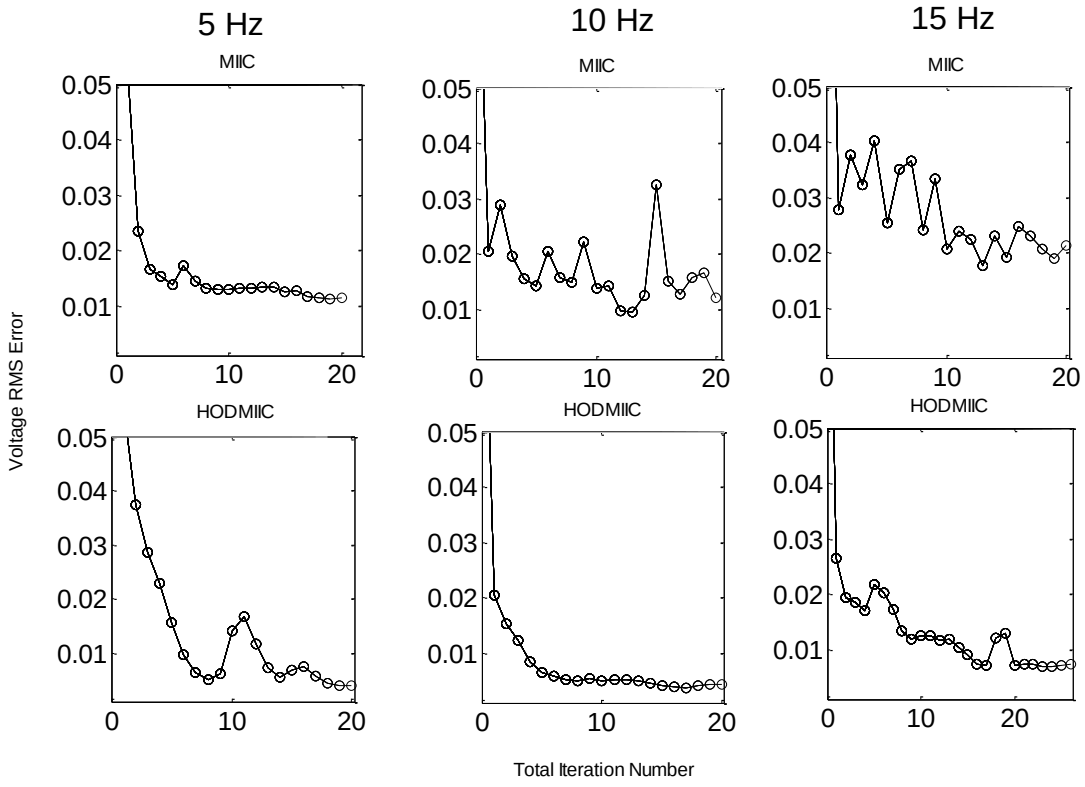


Fig. 31. Comparison of the $E_{rms}$ versus iteration number results as achieved by the MIIC control law (top row) and HODMIIC control law (bottom row) for tracking a 30 $\mu$m amplitude triangle wave from 5 to 15 Hz. Y-axis range is constant between all figures for ease of comparison.

Most of the same comparisons made in the low amplitude control case can be made for this large amplitude control case. With minor exceptions, MIIC and HODMIIC provide the ability for high speed convergence and low error tracking with the RMS errors falling to 0.025 or lower by the fifth iteration of control. HODMIIC even drives some error down as low as 0.01 by the fifth iteration. Again, embedded undulations of

increasing frequency and amplitude are superimposed on the bimorph inputs as the frequency of the desired trajectory increases, showing accurate peak and trough tracking.

Whereas MIIC suffers from a more erratic convergence where error does not monotonically decrease, in general HODMIIC proves superior with a more stable tracking error convergence. The HODMIIC control law also proves superior by achieving overall lower iteration errors than MIIC.

The results for large amplitude, when compared with those for small amplitude, show an interesting change in behavior for the MIIC tracking. MIIC proves more successful at tracking peaks and troughs for a desired triangle trajectory of larger amplitude than for smaller amplitude at the same frequency. Inspection of *Stage* motion during experimentation as well as active monitoring of the motion on an oscilloscope yielded a theory. It appears 30 $\mu$m of amplitude stretches the limits of the system to be tracked successfully at smaller amplitude due to friction. The bimorph is not driven with a large voltage since it is required to only achieve small amplitude of displacement. At these ranges, friction seems to overcome *Stage* motion at the peaks and troughs the desired trajectory where *Stage* velocity approaches a minimum. HODMIIC proves the ability to overcome this issue.

Tracking results are not provided for 250 micrometer amplitude desired trajectories at 25 Hertz because experimentation for this signal was, on a whole, unsuccessful. The believed reason for this sudden inability of both control algorithms to provide tracking links to the previous discussion on sub-harmonics provided in 3.3.3 plant Dynamics. Taking a ¼ multiple of the approximate 80 to 100 Hertz fundamental

frequency results in sub-harmonics of 20 to 25 Hertz. At a frequency of 25 Hertz, *Stage* motion could have been dominated by resonant dynamics and unable to be adequately tracked.

***Dual-Axis Positioning Results***

The control approach to dual axis motion is described in Sec. 3.3.1 *Control Law Implementation*. Considering the superiority of the HODMIIC control law over that of the MIIC, experiments in dual axis control were conducted following the HODMIIC control law. Again, for all experiments, the baseline forgetting factor, $\beta$, was set at 0.03 and the factor $\rho$ was set at 0.05.

Three experiments in total are presented. The desired trajectories employed in all experiments have an amplitude of 250 micrometers. These experiments represent simultaneous motion with identical desired trajectories for both the *X* and *Y Directions*. These desired trajectories are driven at 5, 10, and 15 Hertz.

Fig. 32 shows the experimental tracking and error results using the HODMIIC control law. The first row plots the $E_{rms}$ values for each direction showing the *X Direction* in black and the *Y Direction* in blue. Straight lines connect each iteration data point. A dashed line indicates that the corresponding direction was control-inactive for that iteration and did not receive an updated input. A solid line indicates that the corresponding direction was control active for that iteration and HODMIIC was employed to update the input signal. The three plots of this first row are enlarged and individually presented in the *Appendix F. Dual-Axis Motion Error Plots* for clarity. The

second and third row show zoomed regions of a plot of desired, input, and output signals, the second plot for the *X Direction* and the third for the *Y Direction.* These signal comparison plots are produced after every iteration; however the presented plots represent a single iteration. That iteration which results in the lowest experiment error is presented, whether the lowest error belongs to the *X* or *Y Direction*.

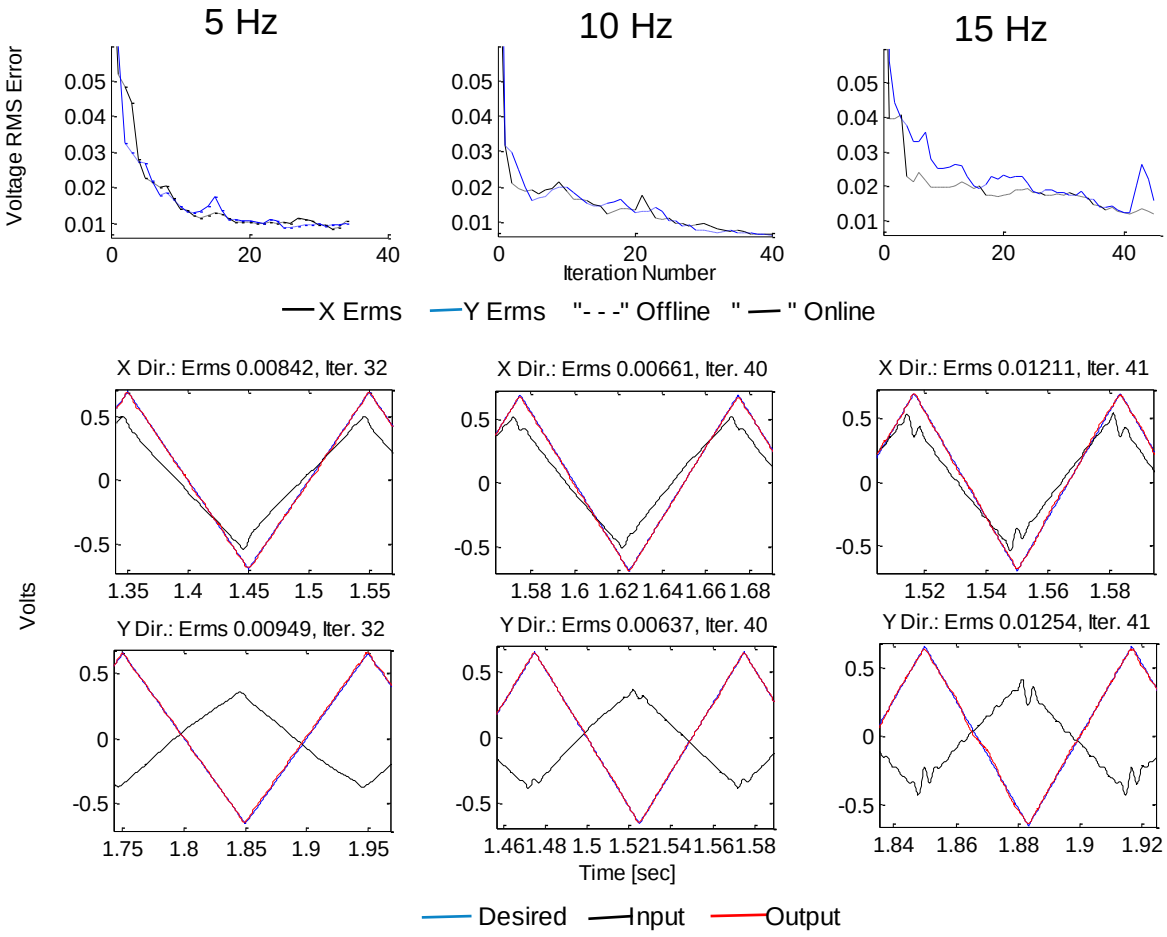


Fig. 32. Experimental results: (top row) Comparison of the $E_{rms}$ versus iteration number results as achieved by the HODMIIC control law for simultaneous X-Y tracking using identical 250 $\mu$m amplitude desired triangle trajectories from 5 to 15 Hz. Error-axis range is constant between all figures for ease of comparison. (bottom rows)

Comparison of the output tracking obtained by the HODMIIC control law for each direction during dual-axis motion of the identical trajectories.

In general, the HODMIIC tracking algorithm has proven ability in controlling dual-axis motion of the *Stage* in addition to its successful control of single-axis control. For each of the presented experiments, it is shown that tracking error can be driven far lower than the error threshold of 0.05. In fact, it is shown possible to drive the error for each direction below 0.01, though at the expense of a high iteration count. The control law proves also to achieve a high convergence speed, as tracking in all cases can be driven sub 0.04, and in most cases sub 0.03, within five iterations.

Through most of the operating range of frequencies, a behavior difference arises between the *X* and *Y Directions* of motion. This is quantified in Table 7 showing the number of total iterations spent under active control for each direction. This iteration total does not include the first iteration, where by convention each direction is forced in control-active mode.

| **Experiment** | **# Iterations of Active Control** | |
|---|---|---|
| | ***X*** | ***Y*** |
| 250 μm - 5 Hz | 15 | 19 |
| 250 μm - 10 Hz | 22 | 18 |
| 250 μm - 15 Hz | 7 | 38 |

Table 7. Number of active iterations for each direction in dual-axis motion HODMIIC control for each of the three experiments.

The *Y Direction* on average has spent much more time under control-active mode than the *X Direction* through these experiments. This could signify less stable system dynamics which occur for the *Y Direction.* These dynamics can be a result of system imperfection, less than ideal bimorph behavior, or even both. One possibility lies in the geometry of the *Stage* design. Considering the *Y Bimorph* tip, more mass is distributed further from each of the bimorphs short faces than for the *X Bimorph.* This is due to the *Stage* geometry being rectangular but not square; the *Stage*s long axis aligns with the x axis and not the y axis. Asymmetry across the y axis then would result in different moments generated by the *Stage* mass and thus a nonzero net moment. This would contribute unwanted dynamics effects.

In addition, bimorph behavior is generally nonlinear and also varies from bimorph to bimorph, as the manufacturing process is not altogether perfect. This may affect the comparatively worse behavior of the *Y Direction,* making it more difficult to control.

# 4. Conclusion

The design and development of mechanical and signal-conditioning electrical systems were presented in detail to achieve the high-precision and low-cost multi-degree of freedom positioning concept for novel introduction to self-assembly-based nanomanufacturing of DNA patterns. The system models were provided for multiple direction of motion and analyses described the difference between the theoretical and actual amplitude and frequency limits for successful tracking of trajectories. It is shown that both the MIIC and HODMIIC control algorithms are capable of tracking one direction of motion to high precision for both large and small triangle wave amplitudes and across low and high frequencies. Both algorithms are capable of achieving an voltage based RMS error well below 0.05. HODMIIC is proven the superior algorithm with successful tracking of high speed and large amplitude trajectories prior to close approach of a range of sub-harmonics which impede tracking success. Specifically, HODMIIC accomplishes successful tracking for dual-axis motion. HODMIIC incorporates a weighted complete history of previous results and is implemented in a novel control architecture to accommodate for dual-axis coupling effects without the need to quantify coupling. These undesirable coupling effects, as well as inherent hysteresis effects and excited vibrational dynamics of the piezoelectric actuator, are shown to be successfully and quickly compensated.

# Appendix A. List of System Components

This is a detailed list of all components labeled in both the Mechanical and electrical system signal flow diagram and the Physical Plant diagram, Figures 1 and 2 respectively of Sec. 2.1 *Overview*.

**Host PC**

The host PC runs Windows 7 operating system and has the MATLAB installed with the Simulink package. There is a direct Ethernet connection between the host PC and the target PC

**Target PC**

The target PC has the Data Acquisition system installed on it via an expansion card slot. The DAQ software boots from a diskette ("floppy disk") read by the computers diskette drive. The DAQ system was a PCI-DAS 1602/16 Analog and Digital I/O Data Acquisition card.

**Shielded Connection Box**

The shield connection box is an SCB-50/BRD manufactured by Measurement Computing. This connection box provides screw terminals for interfacing wires

carrying sensor signals to the target PC DAQ card and wires carrying signals from the DAQ card to the piezo driver/ amplifier.

**Piezo Driver / Amplifier**

A total of three different amplifier channels were employed for this project using two amplifier units, each of which were manufactured by Trek.

- Model PZD350
    - Variable Gain from 0 to 100V/V
    - Max output: 350V
    - One amplifier channel
- Model 603
    - Constant Gain of 50V/V
    - Maximum output: 150V
    - Two amplifier channels

**Physical Plant**

The physical plant hosts the experiments and introduces the desired vibrational motion for the experiment. The list of features is outlined below following their indications on the physical plant representation of Fig. 2.

1. *Stage*
2. *Silicon Chip*

3. *Base*
4. *Bimorph*

   "Stripe Actuator" model 40-2010 manufactured by APC (American Piezo Ceramics) International, Ltd.

   a. *X Bimorph*

      Drives vibration in the *X Direction* shown by the coordinate axes

   b. *Y Bimorph*

      Drives vibration in the Y direction shown by the coordinate axes

   c. *Z Bimorph*

      Drives vibration in the *Z Direction* shown by the coordinate axes

5. *Z Mount*
6. *X, Y Bimorph Clamp*
7. *Reflective Object Sensor*

   Model OPB704 consisting of an Infrared (890nm) Light Emitting Diode (LED) and NPN silicon Photodarlington, manufactured by TT Electronics and distributed by Digi-Key

8. *X Mount*
9. *Threaded Rod*

ASTM A193 Grade B7 Alloy Steel Threaded Rod, ¼" – 20, with a plain finish, distributed by McMaster Carr

*10. Droplet Probe*

*11. Socket Head Cap Screw*

ASTM A574 Grade Black-Oxide Alloy Steel Socket Head Cap Screw, 4-40 partial thread configuration, distributed by McMaster Carr

*12. Hex Nut*

Plain Grade 5 Steel Heavy Hex Nut, ¼" – 20 thread configuration, distributed by McMaster Carr

*13. Hex Nut*

Black-Oxide 18-8 Stainless Steel Machine Screw Hex Nut, 4 – 40 thread configuration, distributed by McMaster Carr

*14. Z Bimorph Clamp*

*15. Z Sensor Rail*

**Power Supply**

The power supply is a triple output power supply model E3630A manufactured by Agilent Technologies. The power supply powers each of the reflective object sensors at 5 VDC and various components of the signal conditioning circuit with a ±~15 symmetrical supply voltage.

**Signal Conditioning**

This electrical circuit conditions the output signal of each reflective object sensor prior to the signals input into the target computer for data collection. The circuit consists of three main blocks. Signal condition is discussed in detail in the electrical design section.

*Signal / Voltage Follower*

Consists of one operational amplifier per input signal. Allows output voltage/signal is able to follow that of the input.

*Level Shifter*

Consists of one operational amplifier per input signal. Adjusting a potentiometer in this sub-circuit enables elimination of the DC offset inherent of the raw sensor signal.

*Active Filter*

Consists of one operational amplifier per input signal. Constructed to provide an active low-pass Sallen filter of second order.

**Oscilloscope**

The oscilloscope is a TDS 2004C series model manufactured by Tektronix. The oscilloscope tapped measurements from various steps of signal conditioning as well as the DAQ and amplifier output at times.

# Appendix B. Reflective Object Sensor

Here is presented further details regarding the final sensor choice, Reflective Object Sensor model OPB704 manufactured by TT Electronics. This model consist of an Infrared (890nm) Light Emitting Diode (LED) and a NPN silicon Phototransistor, mounted side-by-side on converging optical axes in a black plastic housing. A diagram of the model, as provided by the manufacturer, is shown in Fig. 33.

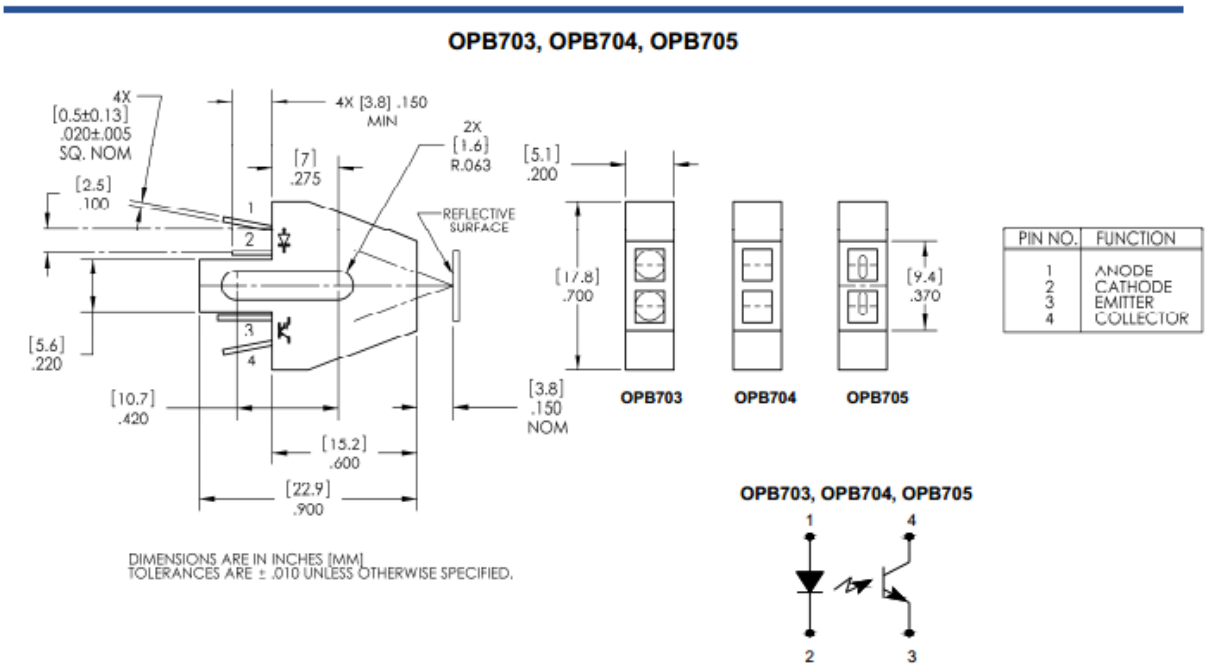


Fig. 33. Dimensions diagram pertinent to the OBP704 reflective object sensor model [18].

The basic sensor operation consists of sending out an optical signal of infrared wavelength and detecting the amount of infrared signal which reflects back to the sensor

off of a reflecting surface of an object. In the figure above, a reflecting surface is shown for example. The output signal from the sensor is a voltage signal, the magnitude of which varies according to the distance between the sensor and reflecting surface. The relationship, as a whole, is nonlinear. However, the relationship contains a fairly large linear range. This linear range was utilized to provide measurements of *Stage* and *Probe* motion.

The two factors effecting sensing system operation, then, were the reflecting surface nominal distance from the sensor, and material of the reflecting surface. The nominal distant is described as the distance between the sensor and reflecting surface when the sensed mass is at its neutral position. For the *Stage*, neutral position implied that the bimorph input signal is zero and the *Stage* has undergone no displacement in the *X Direction* or *Y Direction.* The neutral position is similarly for the *Probe*. The material of the reflecting surface is important since the magnitude of sensor normalized output depends also on the material the IR signal reflects off of, as seen in Fig. 34 as provided by the manufacturer.

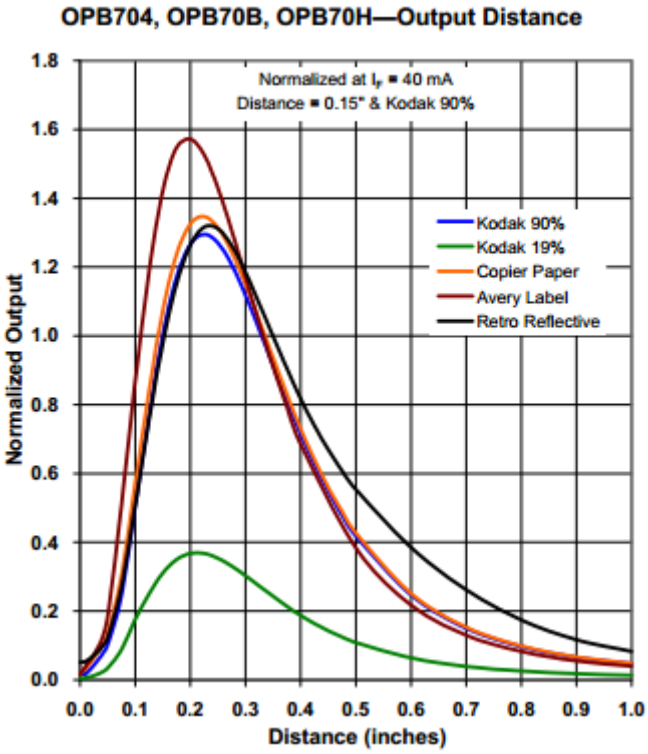


Fig. 34. Normalized output pertinent to OPB704 model as a function of distance being detected and material composing the reflective surface to be sensed [8].

Despite Avery Label paper showing the best reflective surface for the IR signal, for cost and availability purpose, ordinary white printer paper was used for this project and proved to be and adequately reflective material for the sensor IR signal to reflect of off. As was described in post manufacturing processes in Sec. 2.2 *Mechanical Design and Development*, the white paper was cut to size and adhered to the proper reflective surface zones for the *Probe* and *Stage* using double sided scotch tape.

# Appendix C. Operational Amplifier

The final Op Amp choice, OP400, consists of four typical Quad Low Offset, Low Power Operation Amplifiers packed in an integrated circuit chip configuration, as manufactured by Analog Devices. The chip functional block diagram is shown in Fig. 35 as provided by the company.

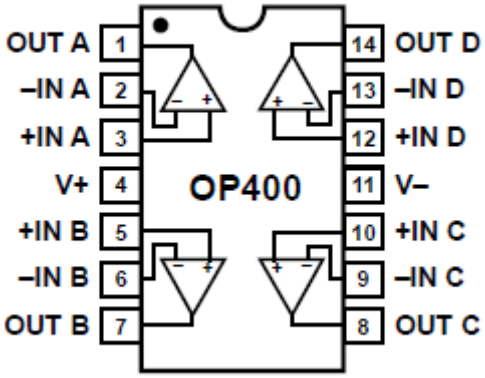


Fig. 35. OP400 Op Amp IC chip functional block diagram [17].

# Appendix D. Level Shifter Design

The basic level shifter configuration is shown in Fig. 36.

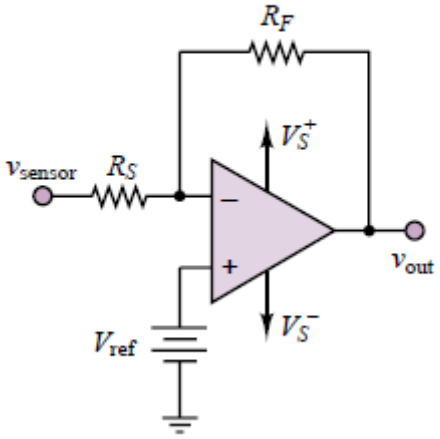


Fig. 36. Level shifter configuration.

We see the sensor signal is connected to the inverting input line and sees an inverting amplifier with gain of $-R_F/R_S$. The voltage source $V_{ref}$ is connected to the non-inverting line and sees a non-inverting amplifier with a gain of $1 + R_F/R_S$. In a closed loop analysis, the superposition principle is applied to yield an expression for the output voltage signal shown in Eq. 19.

$$v_{out} = \frac{-R_F}{R_S} v_{sensor} + \left(1 + \frac{R_F}{R_S}\right) v_{ref} \tag{18}$$

The sensor signal $v_{sensor}$ can be modeled as a sinusoidal wave with some unknown DC signal. Straight substitution, and subsequent rearranging, is represented in Equations 20 and 21.

$$v_{out} = \frac{-R_F}{R_S}[A\sin(\omega t) + DC_{sensor}] + \left(1 + \frac{R_F}{R_S}\right)v_{ref} \tag{19}$$

$$v_{out} = -\frac{R_F}{R_S}A\sin(\omega t) - \frac{R_F}{R_S}DC_{sensor} + \left(1 + \frac{R_F}{R_S}\right)v_{ref} \tag{20}$$

From this representation, the output signal of the op amp has a composite DC offset as outlined. Since the purpose is to eliminate the DC offset, this composite offset must be set to zero, as shown in Eq. 22.

$$DC_{v_{out}} = -\frac{R_F}{R_S}DC_{sensor} + \left(1 + \frac{R_F}{R_S}\right)v_{ref} = 0 \tag{21}$$

This equation can be solved for the required reference voltage value $v_{ref}$ in order to meet the need for offset elimination. The result is Eq. 23.

$$v_{ref} = \frac{R_F}{R_S + R_F}DC_{sensor} \tag{22}$$

A design complication arises in the fact that the DC offset of the input sensor signal is not constant for every experiment. The offset changes according to the nominal distance set between the sensor and the sensing surface. Therefore, since $DC_{sensor}$ can vary, so too must the reference voltage. This adjustable reference voltage is achieved by means of a potentiometer, a form of variable resistor, configured as shown in the final circuit schematic shown previously. The variable resistor acts as an adjustable voltage divider. A 10,000 kilo-ohm potentiometer was used and tied to the same symmetrical supply voltage as the op amps. During experimentation, an oscilloscope is used to monitor the sensor signal before and after *Op Amp LS*. This allows the user to tune the potentiometer resistance via an in-built screw until the output signal of the op amp has a zero DC offset.

The design choice for the level shifter sub circuit involves choosing values for the $R_s$ and $R_F$ resistors. These values affect the gain. In order to simplify circuit design, it was decided that the gain should be applied all at once, as one purpose of the dual-purpose *Op Amp AF*. The choice, therefore, was to choose identical resistance values for $R_s$ and $R_F$ in order to provide a unity gain. The precise value used was a choice guided by practical op amp design considerations. These considerations are as follows:

1) Use standard resistor values
2) Ensure the load current is reasonable by avoiding very small resistance values. As a general rule of thumb, the user should avoid resistance values lower than $100\ \Omega$.

3) To avoid stray capacitance, do not select excessively large resistor values. As a general rule of thumb, the user should avoid resistance values greater than $1\ M\Omega$.

Following these guidelines, $R_s$ and $R_F$, which are shown as $R_3$ and $R_6$ in circuit component table, were chosen to be $5.6\ K\Omega$.

It should be noted that although the gain magnitude was forced to unity, since the signal was an input to the inverting input of *Op Amp LS,* the gain is actually negative in sign, and the output signal is inverted from the input. This will be considered in the following section on active filter and amplification design.

# Appendix E. Active Filter & Amplifier Design

The figure below shows the general Sallen filter setup.

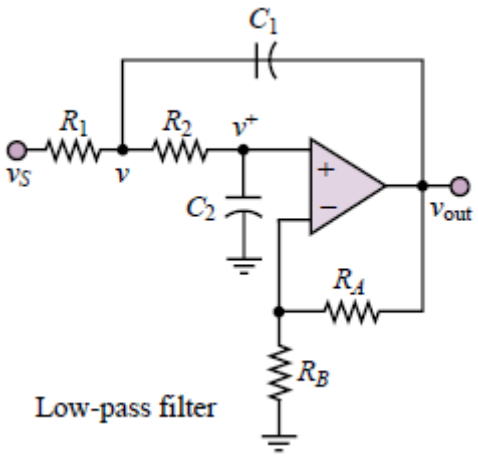


Fig. 37. Sallen filter configuration.

The control of the frequency response is characteristic of three parameters, Quality Factor $Q$, cutoff frequency $\omega_C$, and gain $K$. The quality factor represents the sharpness of the resonant peak in the filter frequency response and is proportional to the inverse of damping. That is, a filter of low damping and therefore high Q will have an underdamped frequency response, and vice versa. For the low pass filter, the cutoff frequency is the boundary between lower frequencies which are allowed to pass through and higher frequencies which are removed from the signal. The expressions showing the relations between these characteristics and the Sallen filter circuit components are shown in Equations 24-26.

$$K = 1 + \frac{R_A}{R_B} \tag{23}$$

$$\omega_C = \frac{1}{\sqrt{R_1 R_2 C_1 C_2}} \tag{24}$$

$$\frac{1}{Q} = \sqrt{\frac{R_2 C_2}{R_1 C_1}} + \sqrt{\frac{R_1 C_2}{R_2 C_1}} + (K-1)\sqrt{\frac{R_1 C_1}{R_2 C_2}} \tag{25}$$

Table 8 shows the final designed gain, cutoff frequency, and inverse quality factor values.

| Parameter | Symbol | Value | Target |
|---|---|---|---|
| Signal Gain | *K* | 2.23 [ ] | *K < 5.7* |
| Cuttoff Frequency | $\omega_C$ | 495 [Hz] | $\omega_C \approx 600$ |
| Inverse Quality Factor | 1/Q | 7.17 [ ] | *5 < 1/Q < 10* |

Table 8. Finalized parameter values for Sallen filter subcircuit.

A very desirable property of the Sallen filter is the fact that the low-frequency gain of the filter is independent to the cutoff frequency and is determined simply by the ratio of resistors $R_A$ to $R_B$. Therefore, the design of these resistor valuers could be completed first, and independently of the cutoff frequency and quality factor. Since the DAQ board has resolution limitations, the outputs sensor signal should be amplified. The amplification has two limitations however. The first has been previously described in the *Index* Sec. 5.4 *Level Shifter Design*. Signal amplification is limited to occur within the bounds of the supply voltage for ideal op-amps, and within bounds reduced by ~1.5 volts for actual op-amps. With a symmetric supply voltage of ±15 Volts, this limits the signal

to the bounds of ±13.5 Volts. The second limitation is the maximum allowed input range to the DAQ card, which is listed by manufacturer specification to be ±10 V. This limitation is the more critical of the two since it the most constricting on the allowed amplification by the *Op Amp AF*. Sec. 2.3.2 described the approximate sensor linear output voltage range from 0.5 to 4 Volts, which is a conservative estimate. This dictates that after removing the DC offset through *Op Amp LS*, *Op Amp AF* would see signal in the range of ±1.75 Volts. Since the objective is to amplify the signal as much as possible within the limits, the maximum allowed gain is $\frac{10}{1.75} \approx 5.7$. The final gain reflected a safety factor and choice of common resistor values.

The cutoff frequency was chosen to be twenty times an absolute maximum operating frequency of 30 Hz. Thus the cutoff frequency goal was 600 Hz.

The last parameter, Quality Factor, was designed by analyzing the frequency response, using the designed cutoff frequency and gain, for several different Quality Factor values. The frequency response model of the Sallen configuration is expressed in Eq. 27.

$$H(j\omega) = \frac{K\omega_C^2}{(j\omega)^2 + (\omega_C/Q)(j\omega) + \omega_C^2} \tag{26}$$

It was found a desireable quality factor would fall between 5 and 10. The choice of $R_1, R_2, C_1,$ and $C_2$ ensued. $C_1$ and $C_2$ were chosen to be identical 0.1 microfarad capacitors for simplicity. An iterative process of choosing $R_1$ and solving for $R_2$ was

used until the values compared closely to known manufactured values and the desired quality factor.

# Appendix F. Dual-Axis Motion Error Plots

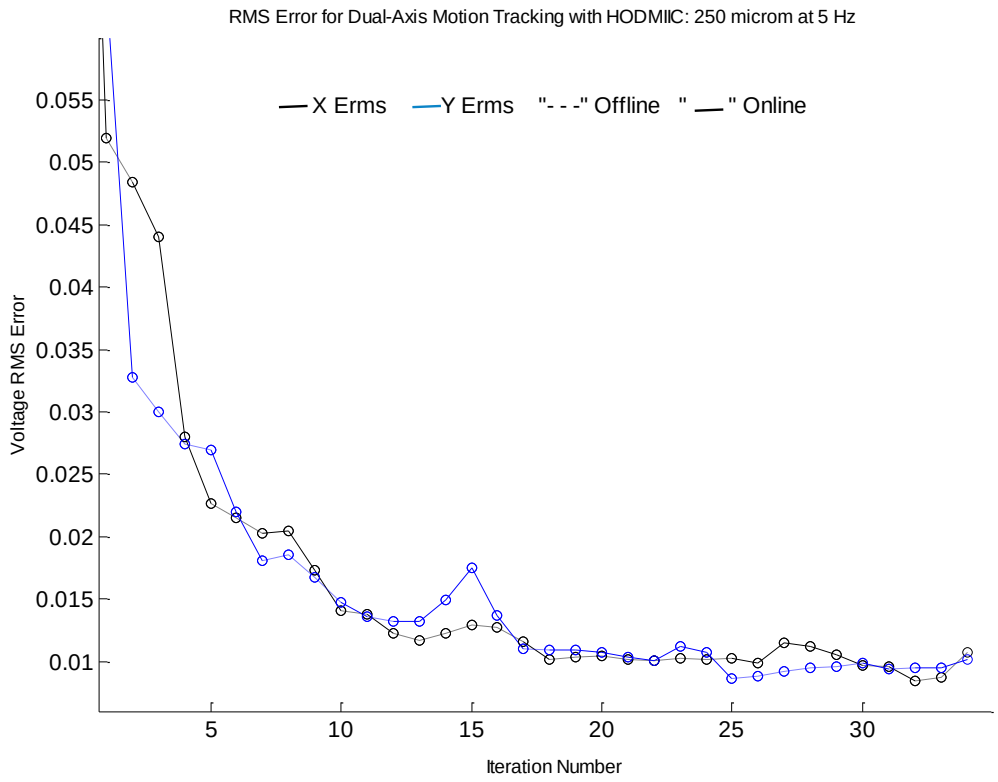


Fig. 38. Comparison of the $E_{rms}$ versus iteration number results as achieved by the HODMIIC control law for simultaneous X-Y tracking using identical 250 $\mu$m amplitude desired triangle trajectories at 5 Hz.

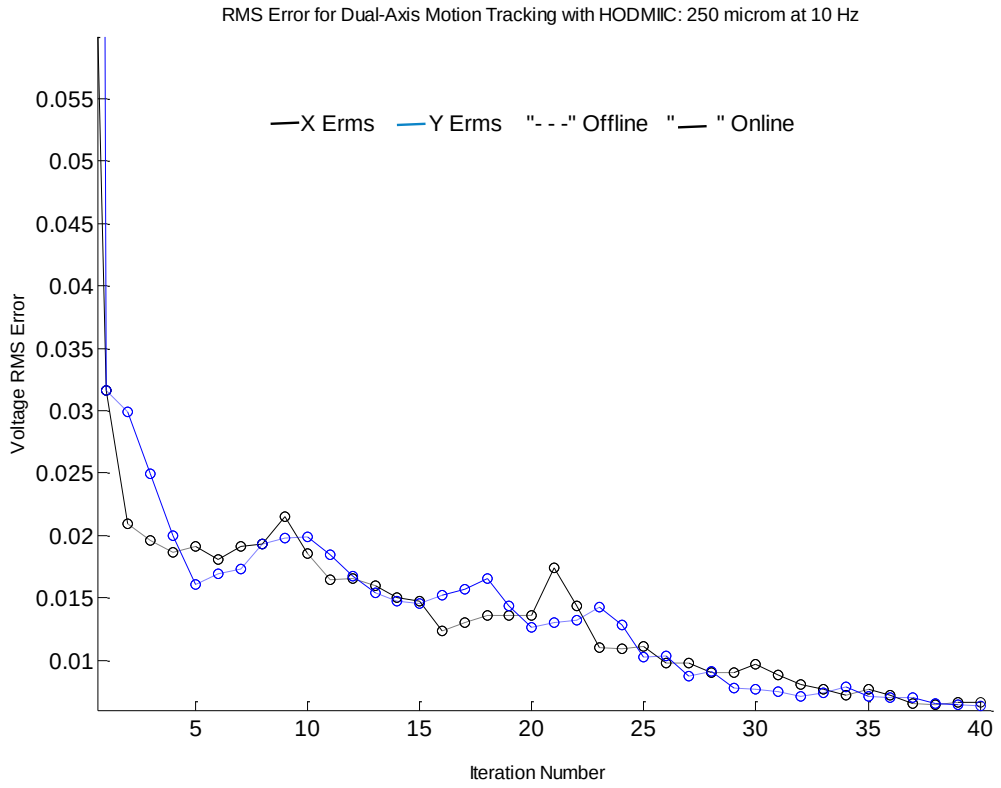


Fig. 39. Comparison of the $E_{rms}$ versus iteration number results as achieved by the HODMIIC control law for simultaneous X-Y tracking using identical 250 $\mu$m amplitude desired triangle trajectories at 10 Hz.

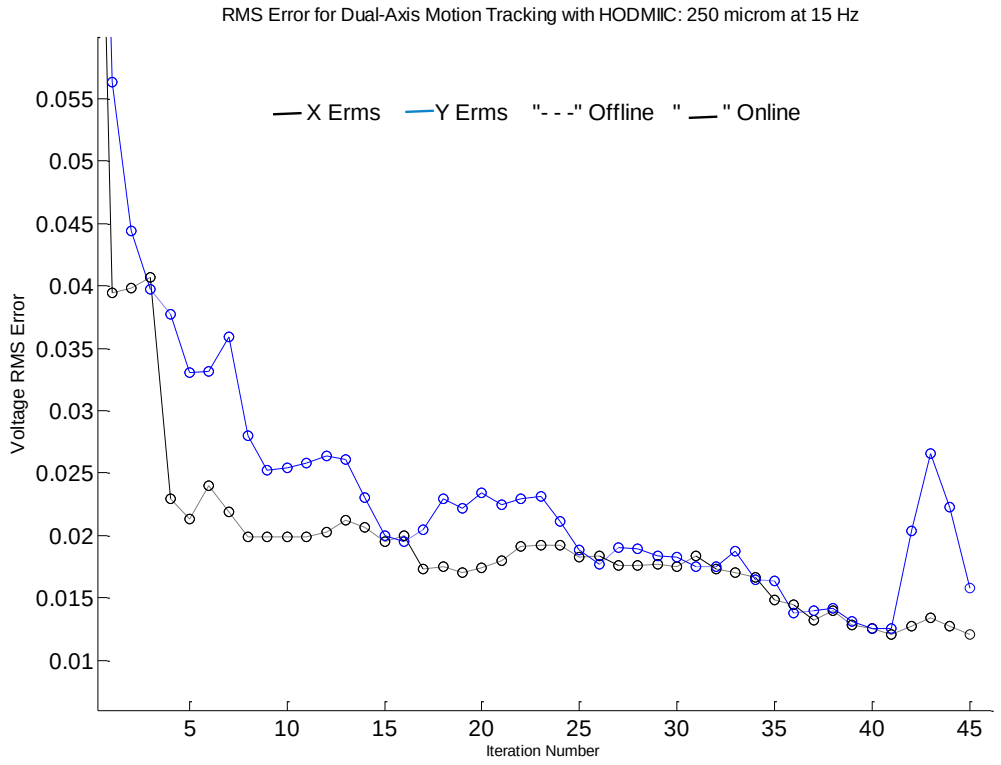


Fig. 40. Comparison of the $E_{rms}$ versus iteration number results as achieved by the HODMIIC control law for simultaneous X-Y tracking using identical 250 $\mu$m amplitude desired triangle trajectories at 15 Hz.

# References


[1] Xu, Jun, Jianfeng Xia, and Zhiqun Lin. "Evaporation-Induced Self-Assembly of Nanoparticles from a Sphere-on-Flat Geometry." *Angewandte Chemie International Edition* 46.11 (2007): 1860-863. Print.

[2] Xu, Jun, Jianfeng Xia, Suck Won Hong, Zhiqun Lin, Feng Qiu, and Yuliang Yang. "Self-Assembly of Gradient Concentric Rings via Solvent Evaporation from a Capillary Bridge." *Physical Review Letters* 96.6 (2006): 1-4. Print.

[3] Govor, L. V., G. Reiter, G. H. Bauer, and J. Parisi. "Nanoparticle Ring Formation in Evaporating Micron-size Droplets." *Applied Physics Letters* 84.23 (2004): 4774-776. Print.

[4] Zhang, Yan. *Inversion*-based *Iterative Feedforward-feedback Control Application to Nanomechanical Measurements and High-speed Nanopositioning*. Thesis. Rutgers University, 2011. N.p.: n.p., n.d. Print.

[5] Wang, Zhihua, and Qingze Zou. "Iterative-Control-Based High-Speed Direct Mask Fabrication Via Ultrasonic-Vibration-Assisted Mechanical Plowing." *6th Annual Dynamic Systems and Control Conference*. Stanford University, Munger Center, Palo Alto. N.p.: n.p., 2013. N. pag. Print.

[6] Yan, Yan, Qingze Zou, and Zhiqun Lin. "A Control Approach to High-speed Probe-based Nanofabrication." *ACC '09: June 10-12, 2009*. Hyatt Regency Riverfront, St. Louis. [Piscataway, NJ]: IEEE. --, 2009. 295-300. Print.

[7] Tien, Szuchi, Qingze Zou, and S. Devasia. "Iterative Control of Dynamics-coupling-caused Errors in Piezoscanners during High-speed AFM Operation." *IEEE Transactions on Control Systems Technology* 13.6 (2005): 921-31. Print.

[8] "Definitions." *Noliac*. Noliac A/S, n.d. Web. 1 June 2011. <http://www.noliac.com/Definitions-679.aspx>.

[9] Wu, Min, Yong He, and Jin-Hua She. "Introduction." Introduction. *Stability Analysis and Robust Control of Time-delay Systems*. Heidelberg: Springer, 2010. 1-18. Print.

[10] Shan, Yingfeng, John E. Speich, and Kam K. Leang. "Low-Cost IR Reflective Sensors for Submicrolevel Position Measurement and Control." *IEEE/ASME Transactions on Mechatronics* 13.6 (2008): 700-09. Print.

[11] J. Li and T.-C. Tsao, "Robust performance repetitive control systems," *ASME J. Dyn. Syst., Meas., Control*, vol. 123, pp. 330–337, Sep. 2001.

[12] M. Butcher and A. Karimi, "Linear parameter-varying iterative learning control with application to a linear motor system," *IEEE/ASME Trans. Mechatronics*, vol. 15, no. 3, pp. 412–420, Jun. 2010.

[13] A. McDaid, K. Aw, E. Haemmerle, and S. Xie, “Control of IPMC actuators for microfluidics with adaptive “online” iterative feedback tuning,” *IEEE/ASME Trans.Mechatronics*, vol. 17, no. 4, pp. 789–797, Aug. 2012.

[14] H. Havlicsek and A. Alleyne, “Nonlinear control of an electrohydraulic injection molding machine via iterative adaptive learning,” *IEEE/ASME Trans. Mechatronics*, vol. 4, no. 3, pp. 312–323, Sep. 1999.

[15] K. L. Moore and J.-X. E. Xu, “Special issue on iterative learning control,” *Int. J. Control*, vol. 73, no. 10, 2000.

[16] Zou, Qingze, and Kyong-Soo Kim. "A Modeling-Free Inversion-Based Iterative Feedforward Control for Precision Output Tracking of Linear Time-Invariant Systems." *IEEE/ASME Transactions on Mechatronics* 18.6 (2013): 1767-777. Print.

[17] "OP400 Datasheet." *Analog.Com*. Analog Devices, 2013. Web. <http://www.analog.com/static/imported-files/data_sheets/OP400.pdf>.

[18] "Reflective Object Sensor OPB703 through OPB705, OPB703WZ through OPB705WZ, OPB70AWZ through OPB70HWZ." *Optekinc.com*. TT Electronics / OPTEK Techonology, Feb.-Mar. 2012. Web. 20 Dec. 2013.